How Caged Motion in the Contact Layer Enhances Thermal Tunneling Across a Liquid/Solid Interface

Hiroki Kaifu and Sandra M. Troian[*]

California Institute of Technology
T. J. Watson Sr. Laboratories of Applied Physics
MC 128-95, Pasadena, CA 91125

Artem I. Baskin

NASA Ames Research Center
Moffett Field, CA 94035

The newest generation of integrated chips for machine learning and artificial intelligence generate enormous power densities, so much so that the extraction of waste heat is now considered the limiting factor in information processing. Although liquid cooled microfluidic networks have been effective in preventing thermal runaway damage, the extracted thermal flux is still limited by the intrinsic thermal slip length at the liquid/solid (L/S) interface, a notoriously difficult quantity to measure at non-cryogenic temperatures. Non-equilibrium molecular dynamics simulations, which are poised to offer a solution, have indicated that a higher liquid contact density corresponds to a smaller thermal slip length due presumably to more frequent L/S collisions. Here we offer a simple but compelling counterexample which challenges this prevailing view. By extracting various metrics relating to the motion of liquid particles in the contact layer, we have uncovered two mechanisms acting in concert which enhance thermal tunneling across the interface despite low contact density. The first requires strong spatial commensurability between the contact layer and surface potential of the adjacent solid. This represses diffusion within the contact layer and intensifies localization by 2D caged motion. Caged particles then tunnel between liquid layers more rapidly thereby shuttling heat toward cooler regions efficiently. Among other results, a smaller thermal slip length correlates positively with a larger non-ergodicity parameter but shorter - not longer - caging time. The fundamental nature of this study suggests a new paradigm for the design of L/S interfaces to maximize thermal transport.

I. BACKGROUND

When modeling thermal transfer at the continuum level across an interface separating dissimilar material, it is normally assumed that at all points of contact, the temperature is equal since the boundary is in a state of local thermal equilibrium [1]. This assumption hinges on whether the thermal boundary resistance (TBR) of the interfacial region is negligible in comparison to that of the adjoining bulk media. When this is not the case, the TBR must be incorporated into the analysis. For two materials in contact subject to a thermal flux J_z (power transfer per unit surface area along the $\hat{z}$ axis), whose surface temperatures maintain a thermal jump $\Delta T = T_1 - T_2 > 0$, the TBR is defined as

$$\mathcal{R} = \frac{T_1 - T_2}{J_z} \ , \tag{1}$$

where for a Fourier conductor

$$J_z = + k(T) \left| \frac{dT}{dz} \right| . \tag{2}$$

Here dT/dz is the local thermal gradient and $k(T)$ the local thermal conductivity, which can only depend on

temperature but not higher gradients. At a liquid/solid (L/S) interface, it is more common to invoke the thermal slip length L_T defined by

$$L_T = \frac{T_1 - T_2}{\left| dT/dz \right|_{liq}} \ , \tag{3}$$

where $|dT/dz|_{liq}$ is the thermal gradient in the liquid interior away from the interface and in the absence of fluid flow. The sketch in Fig. 1 illustrates the geometry which defines L_T as the distance within the solid where extrapolation of the thermal gradient $|dT/dz|_{liq}$ yields the value T_1. Discovery of this temperature jump dates back to P. Kapitza, who in 1941 first measured this discontinuity at an interface separating liquid helium from various metallic solids at cryogenic temperatures [2], thereby introducing the Kapitza length. At non-cryogenic temperatures, it has become more common to refer to this quantity as the thermal slip length, the nomenclature adopted in this work.

The newest generation of integrated chips for machine learning and artificial intelligence generate enormous power densities, so much so that the extraction of waste heat is now considered the limiting factor in information processing. Without rapid extraction of waste heat, densely packed chips easily malfunction from hot spot formation and subsequent thermal runaway. Early studies of heterogeneous bipolar transistors, for example, indicated how current or voltage instabilities generate

———————

[*] Corresponding author:
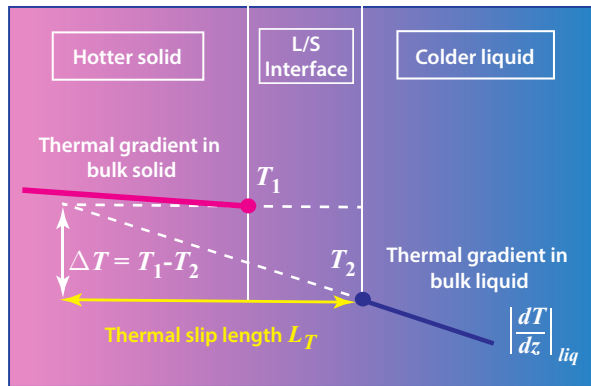stroian@caltech.edu; http://www.troian.caltech.edu

FIG. 1. Schematic diagram (not drawn to scale) illustrating the definition of the thermal slip length $L_T = (T_1 - T_2)/|dT/dz|_{liq}$. With this definition, the extent of the interfacial region is intended to be infinitesimally small in comparison to the thickness of the adjacent solid and liquid layers.

thermal runaway from rapidly increasing junction temperatures [3]. For this reason, the newest generation of compact chips designed for power intensive applications such as data mining and machine learning require single phase liquid cooling. The switch from gas to liquid cooling [4], which relies on circulation of a coolant through a network of embedded microfluidic channels has proven fairly successful in this regard. Even for optimal circulation patterns, however, thermal extraction remains suboptimal due to the intrinsic thermal boundary resistance at the L/S interface, which must be overcome for optimal performance.

A. Predictions of thermal boundary resistance at cryogenic temperatures

Researchers long ago developed two main models for predicting TBR at cryogenic temperatures for systems in which phonons are the dominant heat carrier. The acoustic mismatch model (AMM) assumes specular reflection of phonons at the interface, somewhat akin to specular reflection of electromagnetic waves described by the Fresnel equations. This idealized model overestimates TBR in some systems by over two orders of magnitude (e.g. Fig. 1 in Ref.[5]). Interesting, it also predicts a finite value of TBR for two identical contacting media by virtue of the fact that the interface introduces a discontinuity [5]. The diffuse mismatch model (DMM), which tends to underestimate TBR, assumes all incident phonons undergo scattering at the interface. Generally then, the smaller the acoustic impedance mismatch of the two adjoining materials or the fewer number of surface defects, the smaller the degree of phonon scattering and the smaller the value $\mathcal{R}$ (e.g. Fig. 14 in Ref.[5]). Both the AMM and DMM model suffer from the limitation that the input values to $\mathcal{R}$ rely exclusively on material constants

characterizing the adjoining media and therefore don't incorporate consideration of the interfacial bonding energy or surface defects. Despite these shortcomings, however, at low temperatures below about 30 K, the predictions they yield offer reasonable estimates for solid/solid (S/S) systems when treated to minimize surface defects and pressed together tightly to minimize voids and asperities [6]. Closer to room temperature however, where inelastic phonon scattering and other surface effects play a significant role, neither model provides a reliable estimate of $\mathcal{R}$. Researchers have recently introduced a "phonon model of thermodynamics", an equilibrium based concept able to predict with surprising accuracy over a wide range in temperature and pressure the specific heat of many liquids ranging from noble and metallic to hydrogen-bonded fluids [7]. Whether elements of this successful model can perhaps be extended to non-equilibrium systems maintaining a thermal gradient remains to be seen.

B. Necessity of non-equilibrium molecular dynamics simulations

There exist but a few experimental techniques for measuring TBR or L_T at interfaces in microscale systems due to limitations in resolution and restrictions on the thermal penetration depth of the heat source. Although improvements are underway to enhance measurement sensitivity of the thermal slip length at S/S [8] and L/S [9] interfaces, the latter is particularly challenging at non-cryogenic temperatures. Researchers have therefore come to rely heavily on particle based simulation methods for quantifying thermal exchange across the L/S barrier. In particular, non-equilibrium molecular dynamics (NEMD) simulations are well poised to offer solutions to this challenge. The intermolecular potential of choice for a spherically symmetric two-body interaction of simple neutral particles is the Lennard-Jones (LJ) potential, which has allowed highly accurate predictions of thermophysical values for gaseous, liquid and solid argon. The LJ potential scales as $\varepsilon U(r/\sigma)$, where ε is the inter particle interaction energy, U is the potential function, r is the particle separation distance and σ is the approximate repulsive distance (sometimes called the particle diameter). According to the principle of corresponding states [10], the thermodynamic, structural and dynamic behavior of many other liquids and solids can also be modeled by the LJ potential by different choice of ε and σ - hence, the ubiquitous use of NEMD studies based on the LJ potential [10].

Early NEMD benchmark studies of a bulk homogeneous isotropic fluid confined between two unstructured walls at different temperature confirmed that thermal conduction within the interior liquid and solid is well described by Eq. (2) for fluid density, pressure and temperature ranging from gas-liquid coexistence to the freezing [11] point. With this finding established, researchers began exploring the influence of the L/S interaction en-

ergy ε_{LS} and repulsive distance on the degree of liquid density stratification near a wall, a layering phenomenon first detected in equilibrium systems [12–14]. The first and largest oscillation in the liquid density profile, which always occurs next to the wall, is known as the *contact layer* and its contact density ρ_c determined by integration over that extent of that layer. The value ρ_c should not be confused with the peak density of the contact layer, a local value signifying the maximum amplitude of the first oscillation. As is common, the separation distance between the peak density of the first solid and liquid layers is known as the depletion layer thickness. Subsequent studies unveiled numerous correlations between the thermal slip length in L/S systems and parameters such as the LJ interaction energy [15–20], liquid pressure [21, 22], wall surface temperature [23, 24], wall roughness [20], wall symmetry [25, 26], liquid thickness [27], spring constant used in popular wall-spring models [27] and more. During the last twenty years, NEMD simulations have been extended to the study of structured fluids including hydrogen bonded liquids and solids describing metal, dielectric and insulating material.

C. Importance of the contact layer

Somewhat analogous to the transmission and reflection of light at the boundary separating media of different refractive index, the L/S interface also plays a significant role in regulating the transmission and reflection of thermal energy. As first reported [18, 28], the stronger the L/S interaction energy, the smaller the thermal slip length but the mechanisms responsible for this connection are not well understood. Studies have since attributed this correspondence to an increase in the density of adsorptive/absorptive particles in the contact layer onto the solid surface [29, 30], which some have quantified by the contact density ρ_c [22, 31, 32]. Larger values of the contact density can be had by lowering the system temperature, increasing the liquid pressure or using a denser bulk fluid. It has also been reported in NEMD simulations of L/S systems consisting of water in contact with various orientations of solid silicon that a higher thermal boundary conductance (i.e. lower thermal boundary resistance) [33], which has been attributed to two possible effects. The higher the contact density ρ_c, the denser the first liquid layer and presumably the more frequent the collisions with the solid layer. Secondly, the smaller the depletion layer thickness, the stronger the influence of the corrugations in the solid surface potential, which presumably enhances thermal exchange. Motivated by such findings, NEMD studies have tended to focus on the amplitude, number and character of density oscillations representing the degree of liquid layering against a structured solid. In this work we focus almost exclusively on stationary and dynamic properties associated with the planar (2D) motion of particles within the contact layer.

Subscripts c shall refer to particles in the contact layer and the symbol ∥ to measurements associated with 2D motion in the plane defined by the L/S interface.

D. Organization of paper

The simulations to be described are based on a simple monatomic liquid confined between two identical crystalline walls oriented along one of three facets and whose exterior boundaries are maintained at a given temperature difference. The contact layer temperatures and thermal flux values then vary naturally by different choice of L/S interaction energy and crystal facet. The computational details and methods of analysis used to quantify various stationary and dynamic quantities are detailed in Section II. In Section III, we first benchmark the system by showing how crystal facet orientation, L/S interaction energy and contact layer temperature influence stationary properties such as the liquid density profile, liquid contact density, temperature profiles, thermal flux and thermal slip length. We then examine features of the 2D (i.e. in-plane) radial distribution function and 2D static structure factor describing particle organization throughout the contact layer. This is followed by examination of the 2D and 3D velocity autocorrelation function, 2D mean square displacement and 2D self-intermediate scattering function. The discussion in Section IV focuses on the main finding that a smaller thermal slip length correlates positively with a larger non-ergodicity parameter but shorter - not longer - caging time.

II. COMPUTATIONAL DETAILS

All physical quantities reported in this work are scaled by the reduced units in Table I. The geometry of the multilayer rectangular cell used in the simulations is illustrated in Fig. 2(a) and its dimensions listed in Table II.

As shown, the liquid layer was confined between two unthermostatted solid walls of thickness $L^{hs} = L^{cs}$. The centerline of the liquid layer was positioned at the coordinate origin $z = 0$. Each solid layer acting as the thermal source or sink was placed in contact with a thermostatted solid of thickness $L^{source} = L^{sink}$. All simulations were carried out with thermostat temperatures $T_{source} = 1.6$ and $T_{sink} = 1.0$. Migration or sublimation from the outermost boundaries of thickness L^{fixed} was preventing by affixing those particle in place.

All pairwise interactions between particle pairs $(ij) = LL$, LS or SS were modeled by a truncated and shifted 12-6 LJ potential given by

$$U_{ij}(r) = \begin{cases} U(r) - U(r_c) & \text{if } r \leq r_c, \\ 0 & \text{if } r > r_c \end{cases} \quad (4)$$
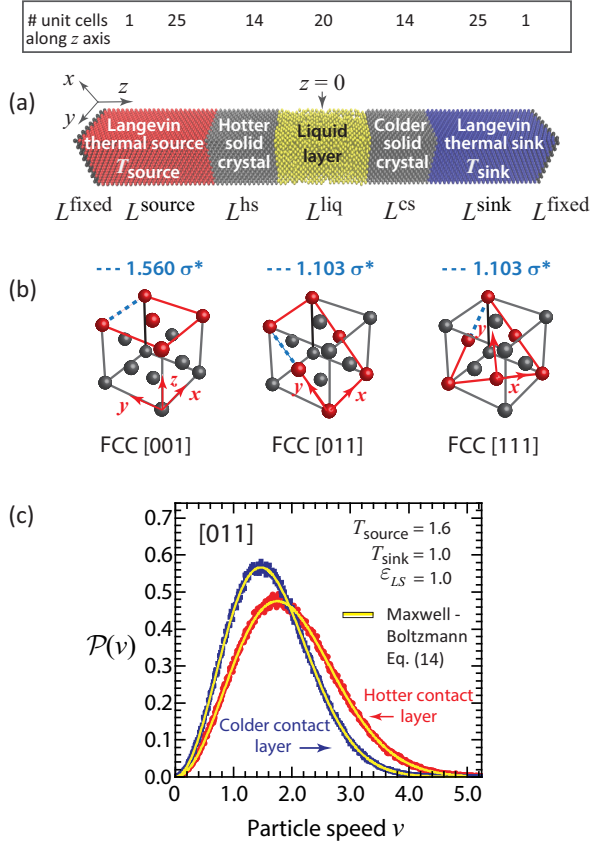
FIG. 2. (a) Layered rectangular computational cell with thermostat source and sink temperatures $T_{\text{source}} = 1.6$ and $T_{\text{sink}} = 1.0$. Listed above the cell geometry are the approximate number of FCC unit cell lengths spanning each layer. (b) Three FCC facet orientations used in this study. Identical facet orientations were imposed on all solid layers. (c) Sample distribution $\mathcal{P}(v)$ showing liquid particle speed inside the hotter and colder contact layer facing an [011] facet for $\varepsilon_{LS} = 1.0$. Superimposed on the data is the Maxwell-Boltzmann distribution function in Eq. (14) for fit constants $T_h^{\text{fit}} = 1.526 \pm 0.001$ and $T_c^{\text{fit}} = 1.0740 \pm 0.0009$.

where

$$U(r) = 4\,\varepsilon_{ij}\left[\left(\frac{\sigma_{ij}}{r}\right)^{12} - \left(\frac{\sigma_{ij}}{r}\right)^{6}\right], \qquad (5)$$

and $r = |\vec{r}_i - \vec{r}_j|$ denotes the particle separation distance, ε_{ij} is the pairwise interaction energy (also called the bonding strength) and σ_{ij} is the separation distance corresponding to $U(r = \sigma) = 0$. The potential cutoff radius was set to $r_c = 2.5$. The truncated and shifted potential guarantees there are no discontinuities in the force field and therefore no impulsive effects which could otherwise influence particle trajectories. Additional key parameters are listed in Table I. For the range of temperature and density in this study, it was confirmed that the interior of the fluid layer remained a well defined dense liquid far from the critical and triple point [36, 37].

To allow propagation of anharmonic modes, all solid

Physical quantity	Numerical value
mass	$m^* = 6.690 \times 10^{-26}$ kg
length	$\sigma^* = 0.3405 \times 10^{-9}$ m
energy	$\epsilon^* = 165.3 \times 10^{-23}$ J
temperature	$T^* = \epsilon^*/k_B = 119.8$ °K
time	$t^* = (m^*\sigma^{*2}/\epsilon^*)^{1/2} = 2.14$ ps
mass density	$\rho^* = m^*/(\sigma^*)^3$
pressure	$p^* = \epsilon^*/(\sigma^*)^3 = 41.7$ N/m^2
effective particle diameters	$\sigma_{LL}^* = \sigma_{LS}^* = \sigma_{SS}^* = \sigma^*$
FCC edge length	$a^* = 1.560\,\sigma^* = 5.382 \times 10^{-10}$ m
interaction energies	$\epsilon_{LL} = \epsilon^*$
	$\epsilon_{LS} = 0.1 - 1.0\ \epsilon^*$
	$\epsilon_{SS} = 10\ \epsilon^*$
Variable	**Value in scaled units**
solid or liquid particle mass 1	
LJ particle diameter	$\sigma_{LL} = \sigma_{LS} = \sigma_{SS}\sigma_{LS} = 1.0$
FCC edge length	$a = 1.560$
integration time step	$\Delta t_{int} = 0.002$
source temperature	$T_{\text{source}} = 1.6$
sink temperature	$T_{\text{sink}} = 1.0$
LJ interaction energy	$\varepsilon_{LL} = 1$
	$\varepsilon_{LS} = 0.1 - 1.0$
	$\varepsilon_{SS} = 10$
bulk liquid density	$\rho_L \approx 0.84$
FCC unit cell density	$\rho_S = 1.0536$

TABLE I. Symbols, numerical values and scalings for non-dimensionalization of physical quantities based on fluid argon [34–36]. Asterisk superscripts signify dimensional quantities. The Boltzmann constant $k_B = 1.380649 \times 10^{-23}$ J/K.

Cell dimensions (scaled by σ^*)	[001]	[011]	[111]
L_x	12.48	12.48	13.24
L_y	12.48	13.24	13.37
L^{fixed} (1 unit cell per end)	1.56	1.10	1.80
L^{source}	39.00	39.71	40.53
L^{hs}	21.84	22.06	21.17
L^{liq}	31.20	30.89	29.72
L^{cs}	21.84	22.06	21.17
L^{sink}	39.00	39.71	40.53
Total length along z axis	156.00	156.64	156.72

TABLE II. Dimensions of the computational cell in Fig. 2(a) (in reduced units).

layers were constructed using the LJ potential in contrast to studies which utilize harmonic wall-spring models. Since the melting temperature of an LJ solid is estimated to be $T_m \simeq \varepsilon_{SS}/0.5$ [38], the S/S interaction en-

ergy was set to $\varepsilon_{SS} = 10$ to ensure those layers remained in the solid state throughout the temperature range explored. At the start of each run, particles comprising all solid layers were situated identically and arranged on the lattice sites of an FCC crystal with unit cell edge length $a = 1.56$ [39]. Each solid layer comprised an integer number of unit cells to prevent overlap of particles along cell edges. The unit cells were oriented with their surface normal representing the [001], [011] or [111] facet oriented along the $\hat{z}$ axis. Dimensions for each orientation are shown in Fig. 2(b). The coordinates of the smallest reciprocal lattice vectors for the real space facet orientations are listed in Table III. Periodic boundary conditions were enforced along the $\hat{x}$ and $\hat{y}$ axes. The L/S interaction strength was varied in increments of 0.1 over the range $0.1 \leq \varepsilon_{LS} \leq 1.0$ spanning behavior from non-wetting to strongly wetting, respectively. Different values of the thermal flux J_z were generated naturally by different choice of L/S interaction energy ε_{LS} and facet orientation. Simultaneous measurements extracted from the colder and hotter side of the liquid layer also allowed examination of the influence of local temperature on various static and dynamic quantities.

FCC facet	$k_{o,x}$	$k_{o,y}$
[001]	± 4.03	± 4.03
[011] (shortest)	± 4.03	0.00
[011] (2nd shortest)	0.00	± 5.70
[111] (quadrants)	± 5.70	± 3.29
[111] (vertical axis)	0.00	± 6.58

TABLE III. Set of shortest reciprocal lattice vectors (RLVs) $\vec{k}_o = (k_x^o, k_y^o)$ (in reduced units) for three FCC facets of a real crystal lattice with unit cell edge length $1.56\sigma^*$. The RLVs for [001] are $(2\pi/a^*)(\hat{e}_x, \hat{e}_y)$, for [011] are $(2\pi/a^*)(\hat{e}_x, 0)$ and for [111] are $(2\pi/a^*)(\sqrt{2}\hat{e}_x, \sqrt{2/3}\hat{e}_y)$ and $(2\pi/a^*)(0, \sqrt{8/3}\hat{e}_y)$. The shortest and 2nd shortest RLVs for the [011] facet are relevant to this study, as discussed in the text.

A. Temperature control

The NEMD simulations were carried out using the open source package LAMMPS [40, 41]. The equations of motion were integrated by the Verlet method [35] based on an time integration step $\Delta t_{int} = 0.002$. Liquid particles, initially situated on the lattice sites of an FCC crystal, were sequentially removed from the fluid layer until the bulk liquid density achieved a value $\rho_{bulk} \approx 0.84$. Particles in the liquid and unthermostatted solid layers were initially equilibrated using a Nosé-Hoover thermostat [42] to a temperature $T_{equil} = 1.3$ for a period $10^5 \Delta t_{int} = 200$. This thermostat was then switched off and two Langevin thermostats [43] then activated and set to the fixed point values $T_{source} = 1.6$ and $T_{sink} = 1.0$

as determined from the Langevin equation:

$$\frac{d^2\vec{r}_i}{dt^2} = -\sum_{i \neq j} \frac{dU_{ij}(r)}{dr}\hat{r}_i - \frac{1}{\tau_{\text{damp}}}\frac{d\vec{r}_i}{dt} + \vec{F}_{\text{stoch}} , \quad (6)$$

where $\vec{r}_i$ is the 3D spatial coordinate of particle i and $\vec{F}_{\text{stoch}}$ denotes a random force vector modeled by a normal distribution of magnitude $[T_{\text{set}}/(\tau_{\text{damp}} \ \Delta t_{int})]^{1/2}$ with set point temperature T_{set}. The damping constant was chosen to be $\tau_{\text{damp}} = 500 \ \Delta t_{int} = 1.0$. After activation of the Langevin thermostats, particles were subject to an additional stabilization period of $2 \times 10^5 \Delta t_{int} = 400$ to ensure steady state conditions. Particle trajectories in the unthermostatted liquid and solid layers evolved according to Newton's equation of motion i.e. Eq. (6) without the damping or stochastic term. The motion of unthermostatted particles therefore derived exclusively from LJ interactions with neighboring particles situated within the potential cutoff radius $r \leq r_c = 2.5$. To ensure proper thermal calibration, it was confirmed that for $T_{\text{source}} = T_{\text{sink}}$, the simulations generated a uniformly flat temperature profile throughout the unthermostatted liquid and solid layers.

The thickness of the thermostatted layers L^{source} and L^{sink}, which ranged from about 39 to 40 (in reduced units), was chosen to exceed the length of a typical phonon mean free path Λ so as to avoid spurious reduction in thermal boundary resistance [44]. It has been shown that for $\Lambda = c_\ell \times \tau_{\text{damp}} \leq 2L_s$, where c_ℓ is the longitudinal speed of sound [22], phonons generated within the thermostatted layers are dissipated before undergoing reflection and propagation from the outer boundary to the L/S interface. Stevens et al. [38] have reported that the value c_L for an FCC crystal is well approximated by the relation $c_l = 9.53\sqrt{\varepsilon_{SS}}$. For the parameter values used in this study, namely $\varepsilon_{SS} = 10$, $\tau_{\text{damp}} = 1$ and $L_s = 39$, the inequality $\Lambda = c_\ell \times \tau_{\text{damp}} = 9.53\sqrt{10} \simeq 30 \leq 2L_s = 78.0$ was well satisfied.

Previous studies in the literature [21, 22] have examined the influence of liquid pressure on the reduction in thermal boundary resistance. We confirmed that the pressure within the bulk liquid was very weakly dependent on FCC facet orientation and not a significant contributor to any reductions in thermal slip length measured. Specifically, the pressures within the bulk liquid for $\varepsilon_{LS} = 0.1$ were measured to be $2.72 \pm 0.03[001]$, $2.78 \pm 0.02[011]$ and $2.86 \pm 0.02[111]$ and for $\varepsilon_{LS} = 1.0$ were measured to be $2.54 \pm 0.02[001]$, $2.60 \pm 0.03[011]$ and $2.66 \pm 0.03[111]$. All things equal, non-wetting fluids gave rise to a slightly higher bulk liquid pressure, as expected. For the density and temperature range explored in this study, it was confirmed that roughly 90% of the bulk liquid pressure stemmed from the virial (not kinetic) contribution.

B. Averaging procedure for time-independent quantities

After thermal stabilization was complete and a steady thermal flux established, averages of various time-independent quantities were carried out as follows. The motion of particles was monitored for a total time $t_{\text{total}} = 5 \times 10^6 \Delta t_{int} = 10^4$, which was divided into ten equal and non-overlapping subdivisions. Within each subdivision, the motion was sampled at intervals of $500\Delta t_{int} = 1.0$ and so the mean values extracted from each subdivision were based on 1000 samplings. This sampling interval was chosen based on inspection of the velocity autocorrelation function, which decayed to zero by $t = 1.0$ (see Fig. 11). In what follows, the reported average values and standard deviations of all time-independent quantities, which are denoted by angular brackets $\langle \cdot \rangle$, were computed by averaging the mean values from each of the ten subdivisions.

Variation of quantities along the $\hat{z}$ axis was obtained by partitioning the unthermostatted liquid and solid layers into non-overlapping bins of volume $L_x \times L_y \times \Delta z_{\text{bin}}$, where Δz_{bin} is the bin width. A very slender bin width $\Delta z_{\text{bin}} = 0.016$ was used in computing density profiles $\langle \rho(z) \rangle$ to ensure resolution of spatial oscillations near the L/S interface indicative of liquid layering. The average density $\langle \rho(z) \rangle$ within each bin was computed from the ratio $\rho_{\text{bin}} = \langle N_{\text{bin}} \rangle / V_{\text{bin}}$, where $\langle N_{\text{bin}} \rangle$ is the average number of particles within a bin. For the values given in Table II, the bin volume corresponding to each facet orientation was 2.49 for [001], 2.64 for [011] and 2.83 for [111]. In this study, the mass density and number density are equivalent since the masses of solid and liquid particles were all set to unity.

A coarser resolution $\Delta z_{\text{bin}} = 0.785$ was used for extracting the temperature distribution $\langle T(z) \rangle$. Too small a bin width causes excessively noisy velocity and thermal profiles from too small values of N_{bin}. It was confirmed that even for the narrowest bin width $\Delta z_{\text{bin}} = 0.016$, $\langle T(z) \rangle$ did not exhibit oscillations near the L/S interface. The average temperature T_{bin} within a bin was extracted from the equipartition relation

$$T_{\text{bin}} = \left\langle \frac{1}{3N_{\text{bin}}} \sum_{i}^{N_{\text{bin}}} \vec{v}_i^2 \right\rangle , \qquad (7)$$

where i denotes a particle within the bin with a (3D) velocity vector $\vec{v} = (v_x, v_y, v_z)$. In computing the thermal gradient within the interior liquid and solid layers and corresponding thermal slip length, only the linear portion of the distribution $T(z)$ away from the L/S interface was fitted.

Temperature jumps at the L/S boundary were extracted from the difference between the temperature profiles linearly extrapolated from the interior solid and liquid layers evaluated at the midpoint of the depletion layer thickness, defined as the distance along the $\hat{z}$ axis separating the peak values in density of the first adjacent solid and liquid layer. As expected, depletion layer thickness was found to vary with ε_{LS}, facet orientation and contact layer temperature. The thermal slip length, measured at both the hotter and colder sides of the liquid layer, was computed from Eq. (3).

In what follows, the *contact layer* refers exclusively to the first layer of *liquid* particles immediately adjacent to the solid surface. The thickness of this layer was measured to be the distance between neighboring minima in $\rho(z)$ bracketing the first oscillation in the liquid density. This distance was evaluated unambiguously because of the distinct stratification in liquid density near the L/S interface for all parameter values explored.

As discussed in Section III, different choices of ε_{LS} and crystal facet orientation naturally yielded different values of the thermal flux J_z, which was evaluated from estimates of

$$J_z = \frac{1}{L_x \times L_y} \frac{E_{\text{net}}(t)}{t} , \qquad (8)$$

where $E_{\text{net}}(t)$ is the net thermal input over a time interval t that was required to maintain the Langevin reservoirs at the set point temperatures T_{source} and T_{sink}. It was confirmed that E_{net} increased linearly in time, as required for steady state conditions. The thermal conductivity values representing the interior liquid and interior solid layers was extracted from the ratio $k = J_z / |dT/dz|$, where the thermal gradient was obtained by a least squares fit over the linear portion of the thermal profile.

Steady state particle distribution patterns within the interior liquid, contact layer and first crystalline layer were evaluated using the static 2D radial distribution function given by

$$g^{\parallel}(r) = \left\langle \frac{L_x \times L_y}{N_{\parallel}} \frac{n_{\text{pairs}}(r)}{2\pi r \Delta r} \right\rangle , \qquad (9)$$

where $N_{\parallel}$ is the number of particles within the selected layer and n_{pairs} is the number of particle pairs within an annulus of radius $r - \Delta r/2 \leq r \leq r + \Delta r/2$ with $\Delta r = 0.01$.

Additional information about long range order within the contact layers was obtained from the static 2D structure factor given by [45]

$$S_c^{\parallel}(\vec{k}) = \left\langle \frac{1}{N_c^2} \sum_{p=1}^{N_c} \exp\left(i\vec{k} \cdot \vec{r}_p\right) \sum_{q=1}^{N_c} \exp\left(-i\vec{k} \cdot \vec{r}_q\right) \right\rangle , \quad (10)$$

where N_c is the number of particles in the contact layer and $\vec{k} = (k_x, k_y)$ is a planar wave vector. Eq. (10) is normalized such that $0 \leq S_c^{\parallel}(\vec{k}) \leq 1$. It was confirmed that within statistical error, contributions from the imaginary part of Eq. (10) were vanishingly small. Results in Section III represent the real contribution to Eq. (10).

Facet	ε_{LS}	$\langle N_c \rangle_{\text{hotter}}$	$\langle N_c \rangle_{\text{colder}}$
[001]	0.1	104.3 ± 0.4	109.9 ± 0.4
[011]	0.1	116.6 ± 0.4	125.3 ± 0.4
[111]	0.1	122.0 ± 0.4	128.6 ± 0.4
[001]	1.0	114.9 ± 0.4	125.0 ± 0.5
[011]	1.0	80.7 ± 0.3	92.9 ± 0.4
[111]	1.0	134.1 ± 0.4	161.4 ± 0.5

TABLE IV. Average total number of particles $\langle N_c \rangle$ in the contact layer at the hotter and colder side for $\varepsilon_{LS} = 0.1$ and 1.0 and three facets.

C. Averaging procedure for time-dependent quantities

Time-dependent and correlated behavior of particles in the contact layer was based exclusively on collections of liquid particles which remained within the layer throughout the entire measurement interval. Particles which exited the contact layer but then returned were excluded from the current analysis. For a given solid facet orientation, it was generally the case that an increase in ε_{LS} or decrease in contact layer temperature led to longer particle residence times.

Once steady state thermal conditions had been established, averages of time-dependent quantities were carried out using the following block averaging scheme. For the first block, tracking of particle trajectories was initiated at data collection times $t_o = (0, 10, 20, \ldots, 475,000) \times \Delta t_{int}$ then subsequently sampled at short intervals $10\Delta t_{int} = 0.02$. Data collection spanned a period $t_o \leq t \leq t_o + t_f$, where t_f was selected to be the longest interval of time during which at least ten particles remained exclusively within the contact layer throughout the period of measurement. For comparison, listed in Table IV are measurements of the average total number of particles within the hotter and colder contact layer for two values of ε_{LS} and the three facets. Therefore, by the time only ten particles from the original occupancy number remained, roughly 90% had exited the layer at least once.

Each initial time for data collection t_o therefore led to slightly different values of t_f. For meaningful averages with a single block, the smallest value t_f was used to compute the time average relevant to the block. A similar procedure was applied to two subsequent non-overlapping blocks, with the first data collection time in the sequence set to the value t_f of the previous block. The smallest overall value t_f recorded for three such blocks was then used to extract the final average reported pertaining to the overall block (B) average. Relations for quantities indicated by the symbol $\langle \cdot \rangle_{t_o,}^B$ therefore denote the final average value based averages over t_o followed by block averaging. In all cases, the time t_f far exceeded the decay time of the velocity autocorrelation function by an order of magnitude.

Dynamic regimes describing different types of particle motion within the contact layer were quantified in two ways. The 2D mean-squared displacement was computed as

$$MSD_c^{\parallel}(t) = \left\langle \frac{1}{N_c} \sum_j^{N_c} \left| \vec{r}_j(t_o + t) - \vec{r}_j(t_o) \right|^2 \right\rangle_{t_o}^B, \quad (11)$$

where $\vec{r}_j(t) = [x_j(t), y_j(t)]$ is the 2D position vector of particle j within the contact layer and $N_c = N_c(t_o, t_f)$ is the number of particles permanently occupying the contact layer throughout the measurement interval $t_o \leq t \leq t_o + t_f$ subject to the constraint $N_c \geq 10$. The 2D self-intermediate scattering function was evaluated according to

$$F_c^{\parallel}(\vec{k}_o, t) = \qquad\qquad (12)$$
$$\left\langle \frac{1}{N_c} \sum_{j=1}^{N_c} \exp\left\{ i\,\vec{k}_o \cdot \left[\vec{r}_j(t_o + t) - \vec{r}_j(t_o) \right] \right\} \right\rangle_{t_o}^B,$$

where $\vec{k}_o$ represents the wave vector corresponding to the first peak in the structure factor. As discussed earlier, $\vec{k}_o$ was found to equal the smallest reciprocal lattice vector except for the [011] case below the structural transition which coincided instead with the second smallest reciprocal lattice vector. The results in Section III represent the real contribution to $F_c^{\parallel}(\vec{k}_o, t)$ - the imaginary contributions were found to be negligibly small by comparison. The velocity autocorrelation function for particles in the contact layer was determined in similar fashion according to

$$VACF_c^{\parallel}(t) = \left\langle \frac{1}{N_c} \sum_{j=1}^{N_c} \vec{v}_j(t_o + t) \cdot \vec{v}_j(t_o) \right\rangle_{t_o}^B. \quad (13)$$

All measurements of quantities reported in this work can be found in Tables VII through IX.

III. RESULTS

A. Thermal equilibrium of the contact layer

Shown in Fig. 2(c) is a sample plot of the particle speed distribution in a hotter and colder contact layer against a [011] facet for $\varepsilon_{LS} = 1.0$. Superimposed on the data are least square fits to the Maxwell-Boltzmann distribution (in reduced units)

$$\mathcal{P}(v_i) = 4\pi \left(\frac{1}{2\pi T} \right)^{3/2} v_i^2 \exp\left(-\frac{v_i^2}{2T} \right) \quad \text{for } i \in N_c, \quad (14)$$

where $v_i^2 = (v_{i,x})^2 + (v_{i,y})^2 + (v_{i,z})^2$. Least squares fits to Eq. (14) yielded the fit constants $T_h^{\text{fit}} = 1.526 \pm 0.001$ and $T_c^{\text{fit}} = 1.074 \pm 0.0009$. The average kinetic en-

ergy in the contact layer, as derived from the Maxwell-Boltzmann distribution, yields the equipartition relation. Least squares fits to Eq. (7) yielded very similar estimates $T_h = 1.529 \pm 0.006$ and $T_c = 1.074 \pm 0.004$, as should be the case.

As expected, the distribution of particle speeds in Fig. 2(c) is broader and the average speed and therefore kinetic energy higher for the particles in the hotter layer. While the overall layered S/L/S system describes a state of thermal non-equilibrium due to the application of a steady temperature gradient, this distribution of velocities confirms that the contact layer is in a state of local thermal equilibrium. It was also confirmed that for the parameter values used in this study, the liquid film remained quiescent and never underwent any convective flow.

B. Characterization of contact layer by time-independent quantities

1. Influence of crystal facet, L/S interaction energy and temperature on contact layer density

It is known from prior molecular dynamics studies of systems in thermal equilibrium [12–14, 46, 47] and non-equilibrium [16, 22, 28, 48–51] that a fluid in contact with a featureless or structured solid will exhibit an oscillatory density profile $\rho(z)$. The characteristic peak to peak separation is normally set by the repulsive part of the inter particle potential. For a sufficiently thick liquid layer, the amplitude and number of oscillations increases at colder temperature or higher values of ε_{LS}, with rapid decay to the value of the interior liquid. These general features are evident too in Fig. 3(a)-(f) showing the influence of ε_{LS}, facet and local temperature on the liquid density profile. The horizontal line is the reference value $\rho = 0.84$ of the interior liquid chosen for this study.

The results in Fig. 3(a)-(f) confirm that the spacing of crystal planes is smallest for the [011] and largest for the [111] facet and that the solid layer peak density is largest for [111] and smallest for [011], in line with the facet dimensions in Fig. 2(b). The degree of liquid layering, indicated by the amplitude and number of oscillations, is smallest for the [011] facet and largest for the [111] facet. This suggests that particles in the contact layer against a [011] facet can move more easily between layers in comparison to comparable particles against the other two facets. We shall return to this point when discussing results extracted from actual particle trajectories. At both the hotter and colder interface, it is apparent that the liquid facing the [011] facet also undergoes a structural transition at some value ε_{LS} which depends on temperature. This abrupt jump, particularly noticeable on the hotter side, is evident from the shift in the location of the first liquid oscillation. For values ε_{LS} above the transition, the depletion layer thickness for the [011] case decreases while that for the [001] and [111] undergo a
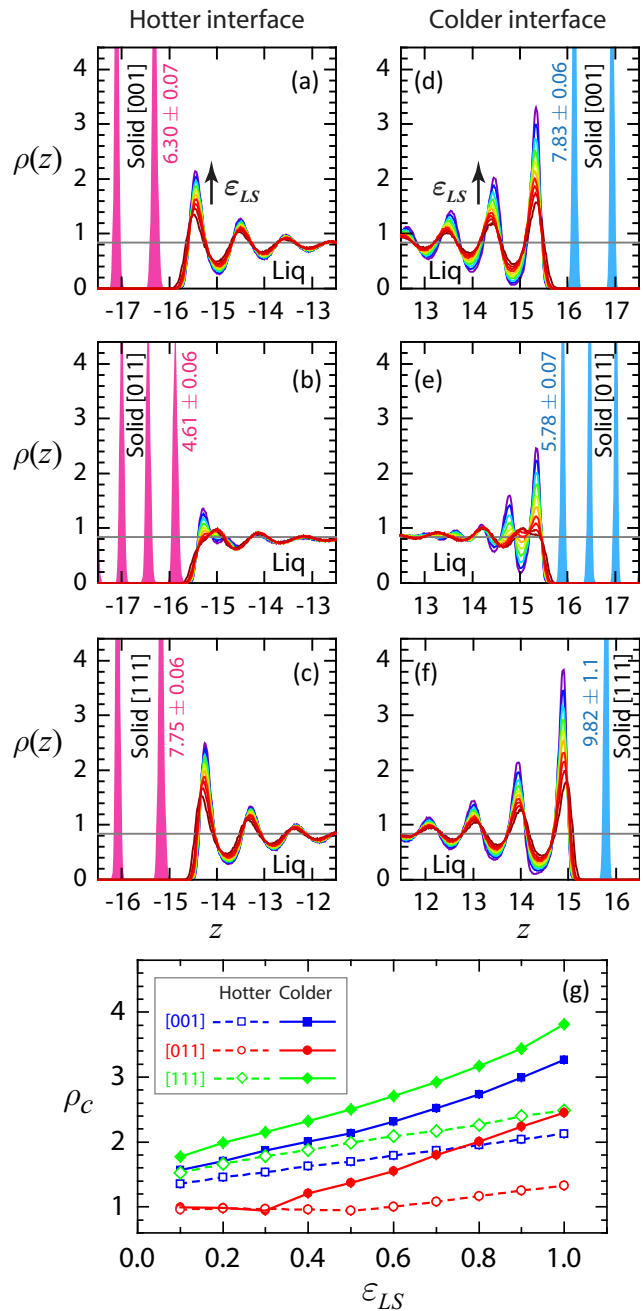

FIG. 3. (a) - (f) Liquid density $\rho(z)$ at the hotter and colder L/S interface for three facets and $0.1 \leq \varepsilon_{LS} \leq 1.0$ in increments of 0.1. Also shown are the first few peaks of the solid density for $\varepsilon_{LS} = 1.0$ (amplitude exceeds plot boundary) and the interior liquid density $\rho_{bulk} = 0.84$ (grey horizontal line). Numerical values listed next to the first solid layer denote the peak solid density (evaluated with bin width $\Delta z = 0.016$). (g) Contact density ρ_c evaluated by integration over the first liquid layer, as described in the text. Error bars are smaller than the line thickness and not visible.

slight increase. That said, the depletion layer thickness for the liquid facing a [011] facet is always the smallest of all facets no matter the value ε_{LS}.

Shown in Fig. 3(g) is the contact density ρ_c for the contact layer facing different facets on the hotter and colder side with increasing ε_{LS}. In all cases, ρ_c rises monotonically with increasing ε_{LS}, although the slope of the rise is highest for colder temperature. In comparing the influence of facet orientation either on the hotter or colder side, for a given value of ε_{LS}, ρ_c is smallest against the [011] facet by a significant amount and largest against the [111] facet. The structural transition noted earlier for the [011] case seems evident here too for $0.3 \lesssim \varepsilon_{LS} \lesssim 0.4$; below this range, ρ_c is rather insensitive to ε_{LS} and temperature.

It is well known that the interfacial energy density (i.e. energy per unit area of the interface) of liquid particles against a structured or unstructured solid wall is comprised of three distinct contributions - namely, the Gibbs surface excess energy, the excess entropy and the excess number of absorbed liquid particles [46]. Although beyond the scope of this current work, quantification of the relative contributions to the interfacial energy density for increasing value ε_{LS}, different facet orientation and different local temperature will provide more insight into the mechanism driving the structural transition of the contact layer for the [011] case.

2. Influence of crystal facet and L/S interaction energy on thermal profiles and thermal flux

Shown in Fig. 4(a)-(c) are the temperature profiles $T(z)$ throughout the liquid and unthermostatted solid layers. The sizeable jumps at the hotter and colder side reflect the influence of thermal boundary resistance at a L/S interface. Away from the interface, the profiles are linear and the thermal gradient therefore constant, confirming the layers are Fourier conductors. Since the interior liquid density depends on temperature and pressure, there is no symmetry about the $z = 0$ axis, as evident. At steady state and in the absence of convective flow, energy conservation requires that the thermal flux J_z be a constant throughout the unthermostatted layers. Therefore, the layer containing liquid must maintain a much larger magnitude of the thermal gradient, since the thermal conductivity of a simple liquid is always much smaller than that of a solid. The results show that the slope of $T(z)$ in the liquid layer increases monotonically with increasing value ε_{LS}, corresponding to smaller values of the thermal jump. Measured values of the thermal flux, thermal gradient and thermal conductivity can be found in Table VII and values of the thermal jump and contact layer temperature in Table VIII. The data confirm that an increase in L/S interaction energy ε_{LS} reduces thermal boundary resistance such that the temperature of the contact layer T_c is closer to the surface temperature of the solid facet. The data also reveal that for a given value ε_{LS}, the thermal jump ΔT is not always higher at the colder interface, as one might intuit naively. In fact, the data in Table VIII confirm that for
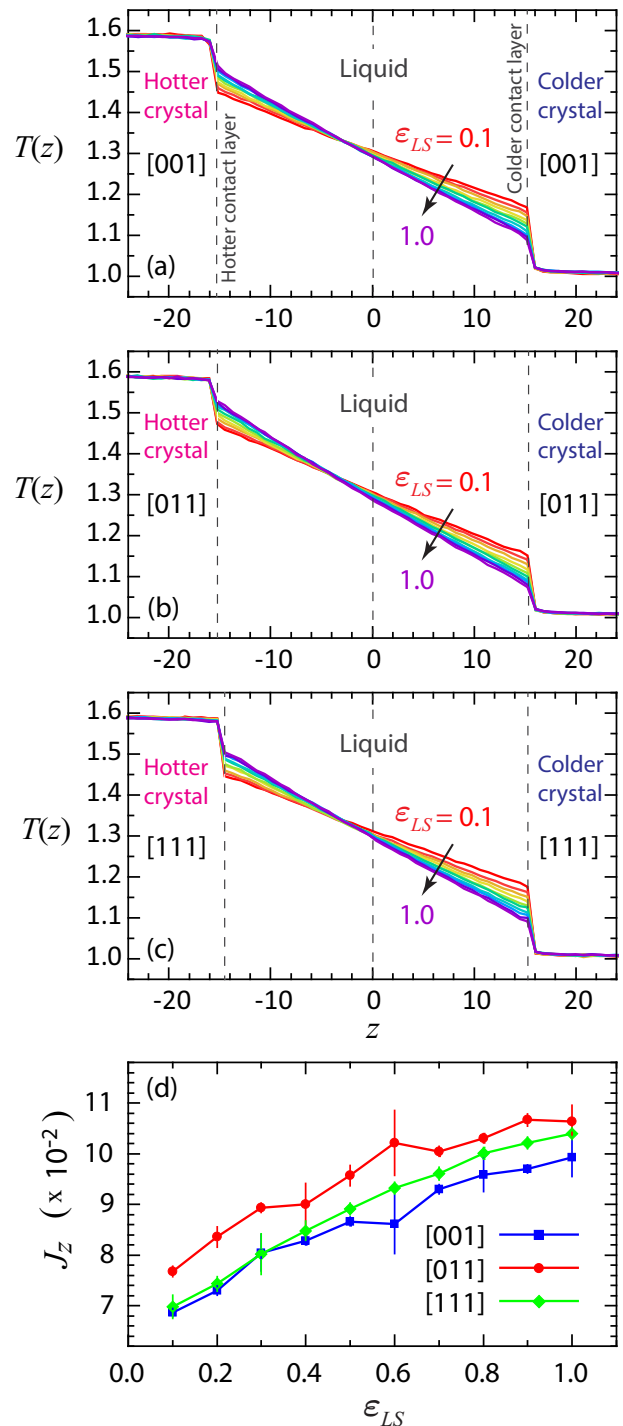

FIG. 4. (a)-(c) Steady state temperature distribution $T(z)$ throughout the solid and liquid layers for three facet orientations and $0.1 \leq \varepsilon_{LS} \leq 1.0$ in increments of 0.1. (d) Corresponding values of the steady thermal flux J_z. Connecting segments are only a guide to the eye.

the same value ε_{LS}, the ratio $\Delta T|_{hotter}/\Delta T|_{colder}$ can be smaller, equal to or larger than one. This is because even for the same value ε_{LS} and same facet, the thermal flux J_z is different due to the influence of local temperature.

It is for this reason that proper comparison between systems of the thermal boundary resistance or thermal slip length requires normalization by the thermal flux, just as indicated by the definitions in Eq. 1 and Eq. (3).

Recall that in this study, the set point temperature of the thermal source and sink were set at $T_{\text{source}} = 1.6$ and $T_{\text{sink}} = 0.6$ for all simulations conducted. The steady thermal flux J_z propagating through the system was therefore not imposed but arose naturally by choice of ε_{LS} and facet orientation. These two input parameters also determined the contact layer temperature. For the geometry used in this study, the L/S interaction energy ε_{LS} and facet choice therefore essentially established "interface filters" which regulated the magnitude of the thermal flux crossing the L/S interface as well as the contact layer temperature. The results in Fig. 4(d) show that for the same value ε_{LS}, the highest thermal flux is achieved with the [011] facet by a significant amount.

3. Dependence of the thermal slip length on L/S interaction energy and contact density

Shown in Fig. 5(a) is the reduction in the thermal slip length, computed from Eq. (3), at the hotter and colder L/S interface, for increasing value ε_{LS} and increasing contact density for the three solid facets. In all cases, the thermal slip length decreases monotonically with increasing ε_{LS}. The reduction in L_T is higher for $\varepsilon_{LS} \lesssim 0.6$ and more gradual above that value showing less sensitivity to ε_{LS} for more wetting liquids. The key result is that for a given value ε_{LS}, the thermal slip length is always smallest for the [011] facet by a considerable amount and largest for the [111] facet. A reduction in thermal slip length as ε_{LS} increases has previously been reported in NEMD studies [18, 19, 51] relying on different thermostatting methods, different L/S media and different parameter ranges, but no general relation proposed. Our data in Fig. 5(a) are well fit by the quadratic relation

$$L_T(\varepsilon_{LS}) = a - b\,\varepsilon_{LS} + c\,\varepsilon_{LS}^2 \;, \qquad (15)$$

indicated by the superposed solid and dashed lines representing least square fits, where a, b and c are positive constants dependent on facet orientation and and T_c. Fit coefficients are listed in Table V.

Shown in Fig. 5(b) is the reduction in L_T for increasing value ρ_c, where of course the value ρ_c cannot be specified but emerges naturally in response to the parameter values input into the simulation. Except for a few notable points, the thermal slip length generally decreases monotonically with increasing value ρ_c, reflecting the influence of the L/S coupling energy. The important result here is that either at the hotter or colder L/S interface, the thermal slip length is smallest for the [011] facet and largest for the [111] facet. The superposed solid and dashed lines indicate least square fits to the reciprocal function

$$L_T(\rho_c) = \frac{\alpha_1}{\rho_c - \alpha_2} \;, \qquad (16)$$

where α_1 and α_2 are positive constants that depend on facet orientation and T_c; fit constants are listed in Table VI. For the [011] facet, the data points for $\varepsilon_{LS} = 0.1, 0.2, 0.3$ on the colder side, and for $0.1 \leq \varepsilon_{LS} \leq 0.7$ on the hotter side deviate more significantly from the reciprocal relation, as indicated by the larger standard deviation values reported in Table VI. As mentioned earlier in this section and to be discussed in more detail in Section III B 5, the contact layer against the [011] facet undergoes a structural transition as a certain value of ε_{LS}, which varies with temperature. The data points in Fig. 5(b) which deviate most from the reciprocal relation in Eq. 16 represent those system below the transition point. This transition induced by the [011] facet was also evident in Fig.3(g) at the colder interface, but less noticeable at the hotter interface where ρ_c is not as sensitive to ε. No similar transition was observed for the [001] or [111] facet for the parameter range in this study.
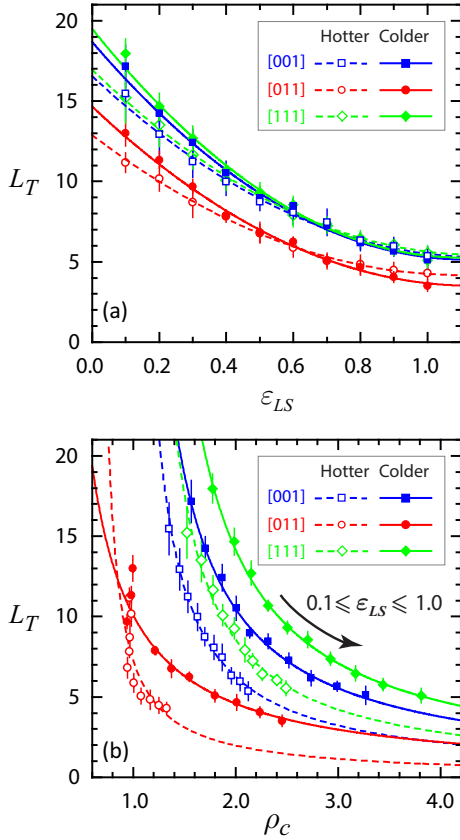

FIG. 5. Reduction in the thermal slip length L_T with (a) increasing L/S interaction energy ε_{LS} and (b) increasing contact density ρ_c at the hotter and colder interface for three facet orientations. Superposed solid and dashed curves represent least squares fit to Eq. (15) and Eq. (16), with fit constants listed in Table V and Table VI, respectively.

Taken together, the results in Figs. 3(g), 4(d) and 5(b) are seemingly counterintuitive. For the same value ε_{LS}, a hotter or colder contact layer against the [011] facet generates the highest thermal flux J_z of all three facets despite having the smallest - not largest - contact density ρ_c . Therefore, a higher contact density does not uniquely predict a higher thermal flux (nor lower thermal resistance or higher thermal conductance), as sometimes suggested [22, 31, 32]. In the original AMM model proposed by Khalatnikov [52, 53], the relation governing the thermal boundary resistance for superfluid helium against a metal surface was shown to depend on several variables such as the local temperature, liquid pressure, elastic properties of the liquid and solid, and the excitation spectra of electrons and different phonon branches of the solid. An increase in one variable can therefore be offset by other factors or confounding variables such that no one variable is a unique predictor of TBR. The results shown in Figs. 3(a) - (f) do suggest that systems with the smallest depletion layer thickness, as for the [011] facet, do appear to maintain the highest thermal flux. Similar behavior [33] has been reported in NEMD simulations of L/S media described by more complex intermolecular potentials describing water on silicon and water on graphene coated silicon; however the depletion length in that study was defined somewhat differently.

Facet	H/C side	a	b	c
[001]	H	16.5 ± 0.5	19.0 ± 2.0	8.0 ± 1.0
[011]	H	12.9 ± 0.2	15.9 ± 0.8	7.3 ± 0.6
[111]	H	16.9 ± 0.3	20.0 ± 1.0	8.7 ± 0.8
[001]	C	18.7 ± 0.6	24.0 ± 2.0	11.0 ± 2.0
[011]	C	14.7 ± 0.5	20.0 ± 2.0	9.0 ± 1.0
[111]	C	19.5 ± 0.6	26.0 ± 2.0	12.0 ± 2.0

TABLE V. Least squares fit coefficients and standard deviation values for parameters a, b and c in Eq. (15).

Facet	H/C side	α_1	α_2
[001]	H	11.8 ± 0.4	0.88 ± 0.04
[011]	H	8.40 ± 1.0	0.17 ± 0.12
[111]	H	14.2 ± 0.3	1.00 ± 0.02
[001]	C	6.60 ± 0.2	0.94 ± 0.02
[011]	C	2.70 ± 0.9	0.63 ± 0.12
[111]	C	8.03 ± 0.4	1.03 ± 0.04

TABLE VI. Least squares fit coefficients and standard deviation values for parameters α_1 and α_2 in Eq. (16).

4. 2D radial distribution function of contact layer and first crystal plane

Shown in Fig. 6 are the 2D radial distribution functions $g^{\|}(r)$ for particles in the contact layer at the hotter and colder interface for three facet orientations with increasing value ε_{LS}. Also superimposed are the results for the first crystal plane for $\varepsilon_{LS} = 1.0$ and the interior liquid. It was determined (not shown) that $g^{\|}(r)$ within the interior liquid and first crystal plane varied weakly with ε_{LS}. The lack of sensitivity to ε_{LS} of the interior liquid region is likely due to the fact that the layer thickness was fairly large and the interior region therefore well shielded from the L/S interface. We also recall that the crystal solid used in this study was constructed using large ratios $\varepsilon_{SS}/\varepsilon_{LS}$ of the order of 10 to 100, thereby reducing sensitivity of $g^{\|}(r)$ for the first crystal plane to changes in ε_{LS}.

As expected, the colder the interface temperature and the stronger the L/S coupling, the stronger the commensurability between the radial distribution of particles within the contact layer and those of the adjacent crystal facet. For the [011] facet, comparison of the distribution function $g^{\|}(r)$ between the contact layer and interior liquid reveals that at smaller values ε_{LS}, the location and shape of the first two liquid peaks almost superimpose, with a small but gradual increase in the mismatch as r increases. This indicates that the local spatial distribution of particles in the contact layer is more isotropic and more liquid-like than for the contact layers against the [001] and [111] facet. This is especially evident for the colder contact layer for $\varepsilon_{LS} \leq 0.3$ and the hotter contact layer for $\varepsilon_{LS} \leq 0.7$. Notably, this is the same parameter range which we noted earlier gave rise to the deviations in the reciprocal functions shown in Fig. 5(b). Also evident from Fig. 6 is that while the contact layer against the [001] and [111] facet undergoes a smooth and gradual increase in $g^{\|}(r)$ as ε_{LS} increases, the layer against the [011] facet manifests an abrupt jump in behavior, indicative of the structural transition noted earlier.

5. Static 2D structure factor of contact layer

The results in Fig. 7 for the static 2D structure factor given by Eq. (10) provide additional insight into the degree of commensurability between the organization of particles in the contact layer and first crystal plane. The logarithmic color scale in Fig. 7 spans three orders of magnitude. Generally, for the same value ε, the colder the contact layer, the closer the structure factor resembles that of the crystal facet, as indicated by the set of discrete points reflecting the maxima. The hotter the contact layer, the more fluid-like the particle packing, as indicated by the circular ring patterns. For all facets, the hotter contact layers for $\varepsilon_{LS} = 1.0$ show stronger commensurability with the underlying crystal facet than do the colder contact layers for $\varepsilon_{LS} = 0.1$. Most notably,
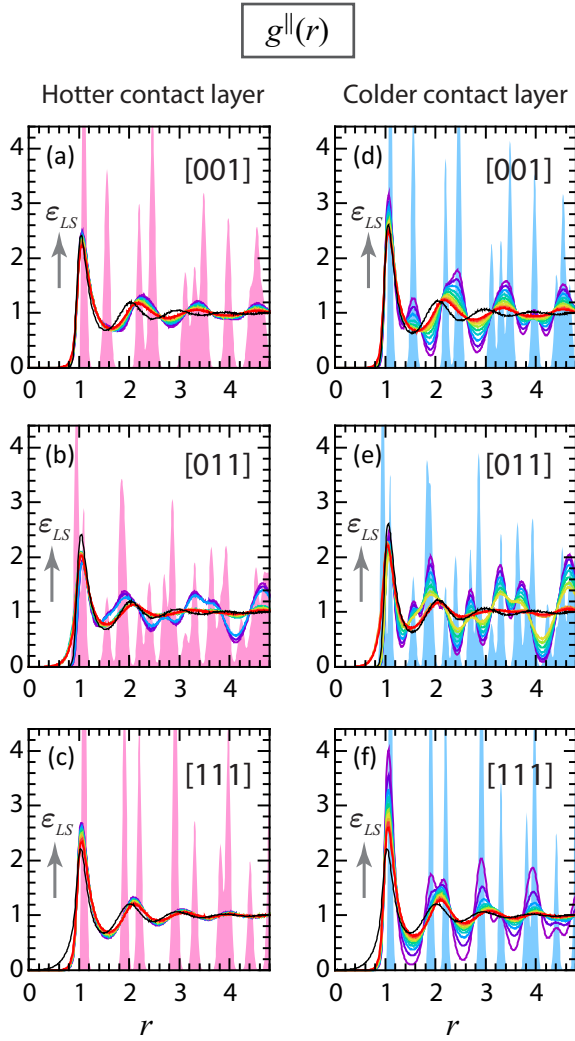
FIG. 6. (a) - (f) 2D radial distribution function $g^{\parallel}(r)$ given by Eq. 9 for the hotter and colder contact layer (colored curves) for $0 \leq \varepsilon_{LS} \leq 1.0$ in increments of 0.1 and three facets. Shown for comparison is the distribution for the interior liquid (black curve) as well as the first crystal plane for $\varepsilon_{LS} = 1.0$ (red and blue shaded peaks).

for either $\varepsilon_{LS} = 0.1$ or 1.0, the [011] facet always induces much longer-range translational order within the contact layer than do the other two facets.

Closer inspection of the images in Fig. 7 and other images for different values of ε_{LS} (not shown) reveals that while the global maxima (small red solid dots) of $S_c^{\parallel}(k_x, k_y)$ for the [001] or [111] case always align with the wave vectors defining the shortest RLVs, the [011] case behaves differently due to the structural transition noted earlier. For $\varepsilon_{LS} = 0.1$, which is below the transition value, the maxima of $S_c^{\parallel}(k_x, k_y)$ coincide not with the smallest but the second smallest RLVs, specified in Table III). For $\varepsilon_{LS} = 1.0$, which is above the transition, the maxima occur at the the shortest RLVs of the crystal facet. Based on a review of the data for all choices ε_{LS},

the real space configuration of particles in the colder contact layer is characterized by a preferential alignment of particles along the $\hat{x}$ axis for $\varepsilon_{LS} \leq 0.3$ and preferential alignment along the $\hat{y}$ axis for $\varepsilon_{LS} \geq 0.4$. This switch in alignment also occurs within the hotter layer in crossing the value $0.7 \leq \varepsilon_{LS} \leq 0.8$. This additional information further informs the trends noted earlier in Sections III B 3 and III B 4.

The maxima of $S_c^{\parallel}(k_x, k_y)$, denoted by $S_{max} = S_c^{\parallel}(k_{o,x}, k_{o,y})$, are plotted in Fig. 8 for increasing value ε_{LS}. For the [111] case, the results show greater sensitivity to ε_{LS} for the colder layer, as expected. Also, while S_{max} for the [001] and [111] facets shows a smooth and gradual increase with increasing ε_{LS}, the [011] case manifests sizeable jumps at $0.7 \leq \varepsilon_{LS} \leq 0.8$ in the hotter layer and at $0.3 \leq \varepsilon_{LS} \leq 0.4$ for the colder layer. These jumps correspond exactly to the switch in particle alignment which occurs for liquid particles against the [011] facet. Above the transition, the values S_{max} for the [011] case always and significantly exceed the values for the other two facets. Therefore particle alignment along the $\hat{y}$ axis reflects much stronger commensurability with the periodic pattern set by the corrugation of the crystal surface potential. Below the transition value, S_{max} for the colder layer against the [001] facet slightly exceeds that for the [011] facet but this difference altogether disappears at higher temperatures.

C. Characterization of contact layer by time-dependent quantities

1. 2D mean squared displacement of particles which never leave the contact layer

Shown in Fig. 9 are sample snapshots from individual runs of the location of particles in the hotter and colder contact layer for two values of ε_{LS} and three facet orientations. The time t_{exit} denotes the instant after which one of four randomly tagged particles escaped the contact layer. Accurate inferences about particle motion and dynamics, of course, requires extensive ensemble averaging, as discussed in Section II. However, the instantaneous snapshots from a single run nonetheless reveal a few interesting trends, later supported by proper ensemble averaging as discussed later in this section.

For a given facet with $\varepsilon_{LS} = 1.0$, a colder contact layer maintains a higher liquid surface density and longer particle residence times, as expected. Also, such layers more strongly adopt the dimensions and symmetry of the adjacent crystal surface potential, an effect which is not as evident to the eye for $\varepsilon_{LS} = 0.1$. For $\varepsilon_{LS} = 1.0$, perhaps the most interesting feature is that particles against either the hotter or colder [011] facet undergo the shortest displacement from their initial position, likely indicative of tighter binding with the solid surface, and yet experience the *smallest residence times* in comparison to the results for the other two facets. This tentative obser-
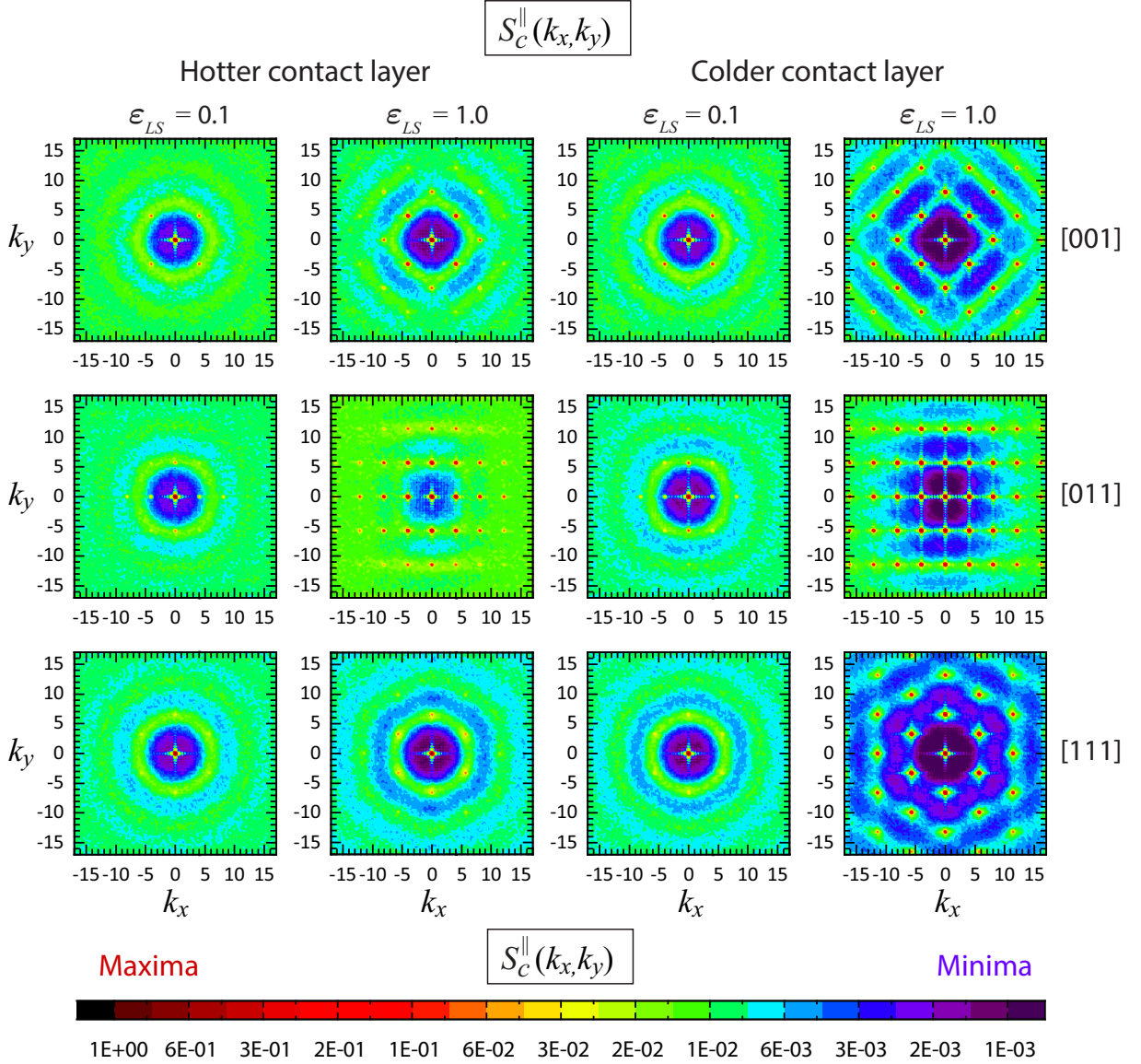
FIG. 7. Static 2D structure factor $S_c^{\parallel}(k_x, k_y)$ [Eq. 10] for the hotter and colder contact layer for two values of L/S interaction energy and three facet orientations. Maximal values appear as small solid red dots.

vation, based only on a few single snapshots, suggests that particles against the [011] facet more readily escape the layer perhaps in response to hindered diffusion in-plane. In what follows, we support this hypothesis with a more comprehensive set of data extracted from many more particle trajectories, which are properly ensemble averaged.

Some key features of the contact layer become evident when examining temporal correlations obtained by extensive ensemble and block averaging of single particle trajectories. Shown in Fig. 10 is the 2D mean square displacement $MSD_c^{\parallel}(t)$ plotted on logarithmic axes for particles in the hotter and colder contact layer for three facet orientations and $0.1 \leq \varepsilon_{LS} \leq 1.0$. These results are exclusively based on particles which never left the con-

tact layer throughout the measurement interval shown. As described in Section II C, the measurement interval was terminated once fewer than ten particles satisfied that minimum occupancy condition. Runs conducted with different input parameter values therefore yielded different terminal times.

The superposed lines in Fig. 10(a)-(f) signify the theoretical exponents for the early (E) and late (L) time motion of a particle in a bulk homogeneous isotropic fluid far from any boundary or interface. These exponent values describe ideal ballistic motion ($\gamma_E = 2$) and diffusive motion ($\gamma_L = 1$). In all cases for the system under study, the influence of the crystal surface potential diminishes the magnitude of these exponents, as evident in Fig. 10(g). In Table IX, the exponents for γ_E were extracted from least square fits over the interval $0.02 \leq t \leq 0.10$ and
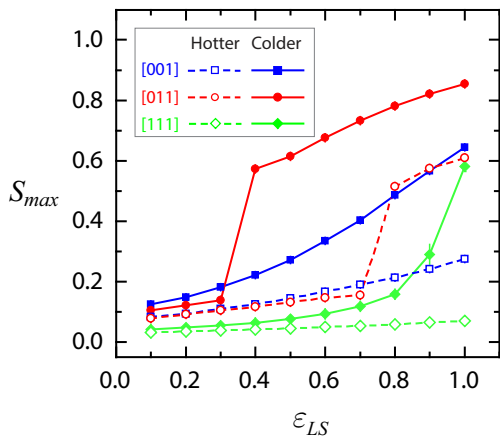
FIG. 8. Maxima of the static 2D structure factor S_{max} extracted from Eq. (10) for particles in the hotter and colder contact layer for three facets and $0 \leq \varepsilon_{LS} \leq 1.0$ in increments of 0.1. Connecting segments are only a guide to the eye. Coordinates of the relevant reciprocal lattice vectors are listed in Table III.

for γ_L over the interval spanning the last decade in time. For motion showing plateau-like response following the (sub) ballistic regime, as observed for the colder [011] facet for $\varepsilon \geq 0.4$ or hotter [011] facet for $\varepsilon \geq 0.8$, the least squares fits were extracted using only the last half-decade. This is because for some parameter values, the plateau-like regime extended only a short period and it was preferable in extracting exponent values to use the same interval in time. Nevertheless, it is clear that the 2D mean square displacement of particles against the [011] facet exhibits the largest departure from the ideal value $\gamma_L = 1$, reflecting a significant retarding influence from the crystal surface potential.

The results in Fig. 10 confirm some interesting features. The behavior of particles against the [001] and [111] facets show a smooth transition from sub-ballistic to sub-diffusive motion, with a gradual reduction in the magnitudes of γ_E and γ_L with increasing value ε_{LS}. By contrast, particles against the [011] facet experience a significant slowdown following the sub-ballistic regime, with a notable drop in the value γ_E exactly at the values of ε_{LS} where there occurs a structural transition discussed earlier. The motion both prior and subsequent to this transition is indicative of 2D caged motion whereby longer excursions from diffusive-like motion are severely repressed. Below the transition in ε_{LS}, caged motion is weaker. Above the transition, particle localization is enhanced and caging quite strong. Against the colder [001] and [111] facets, one also observes a small transient slowdown in mean square displacement quickly followed by a longer sub-diffusive regime. The caged motion induced by the colder [001] and [111] facets is very weak, even for the largest values of ε_{LS}.

The fitted power law exponents plotted in Fig. 10(g) and tabulated in Table IX reveal some interesting features. For all parameter ranges tested, the exponents γ_E, which span the limited range $1.83 \lesssim \gamma_E \lesssim 1.90$, are always smaller than the ideal value 2.0. The motion of particles in the contact layer is therefore slowed in comparison to ideal ballistic motion in a simple homogenous fluid but not by much. Furthermore, the values γ_E are relatively insensitive to facet orientation and temperature and exhibit only a slight decrease as ε_{LS} increases. This minor reduction in exponent is expected since ballistic-like motion is by its very nature inertia-dominated [54] and therefore should not be as sensitive to the influence of the crystal surface potential. For a simple bulk homogenous and isotropic fluid, the mean square displacement in the ballistic regime scales according to $T \times t^2$ (i.e. $(k_B T/m)t^2$ in dimensional units). (Incorporation of hydrodynamic memory effects [55, 56] is known to alter this relation slightly such that the particle mass m is replaced by a slightly larger effective mass to account for the fraction of surrounding fluid displaced by the motion of the particle.) The entries in Table IX and corresponding values of the contact layer temperature T_c in Table VIII confirm that hotter particles undergo larger mean square displacement even in the presence of a corrugated surface potential for the values ε_{LS} tested.

As shown in Fig. 10(g), the exponents γ_L span a much wider range and they too fall below the ideal value 1.0. At late times then, particle motion in the contact layer experiences significant slowdown due to the influence of the periodically corrugated crystal surface potential. For similar parameter values, liquid particles against the [011] facet undergo the smallest 2D mean square displacement, while particles against the [111] facet undergo the largest. Below the structural transition in ε_{LS} for particles against the [011] facet discussed earlier, the values γ_L manifest sizeable jumps. Together with the results in Fig. 8, this implies that the longer range the 2D structural order, induced by colder temperature and/or larger values of ε, the smaller the 2D mean square displacement. Clearly, the hindrance or suppression of 2D diffusive-like motion in the contact layer is caused by significant energy barriers established by the corrugated crystal surface potential.

The caged motion inferred from γ_L for the [011] case, especially notable above the structural transition, can also be seen in Figs. 10 (b) and (e), where there occurs a distinct plateau-like region with a small or vanishing slope. For the colder layer at higher values of ε_{LS}, the 2D mean square displacement practically stalls due to significant particle localization. This behavior spans about one decade in time for the hotter layers and almost two decades in time for the colder layers. Near $t \gtrsim 10^{-1}$ for larger values of ε_{LS}, the motion briefly reverses as particles undergo recoil within dynamic cages just prior to onset of the 2D caged regime. At higher temperatures and smaller values of ε_{LS}, this recoil is far less pronounced.

Generally, the terminal time increases as ε_{LS} increases. This is expected since larger L/S bonding energy should cause more particles to remain situated within the con-
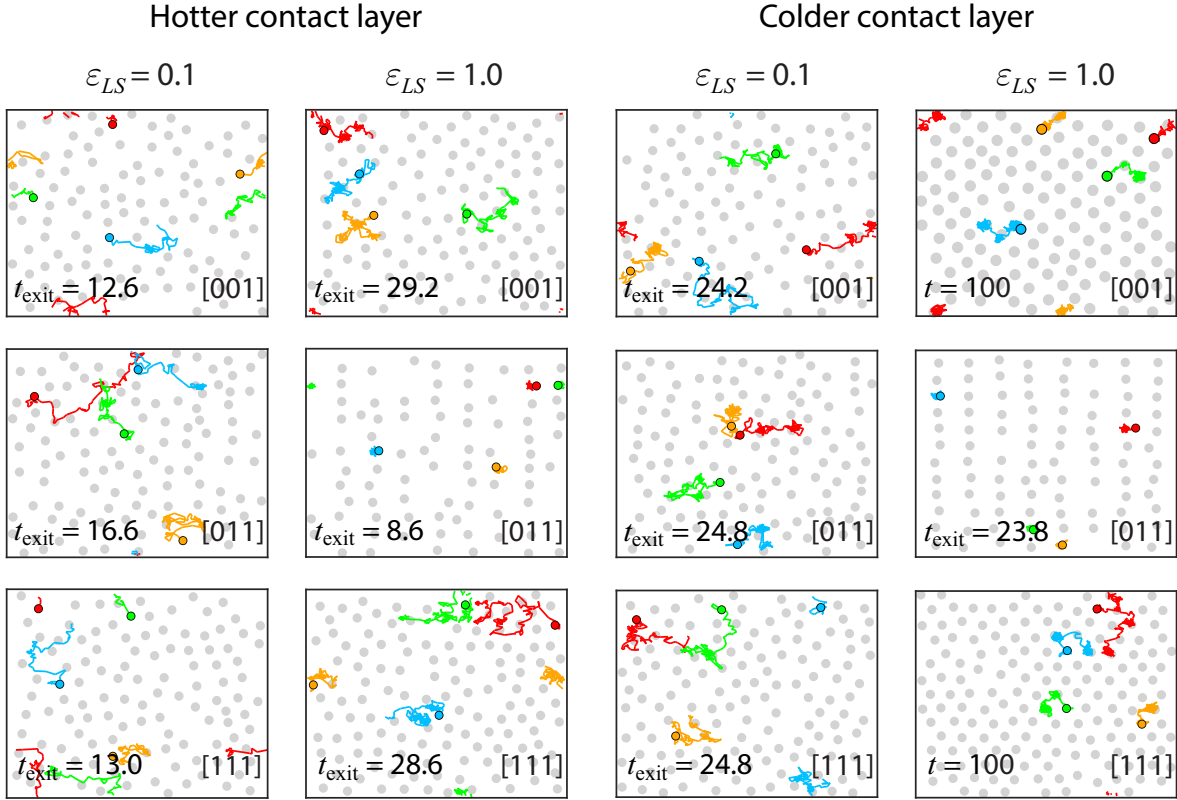
Hotter contact layer

Colder contact layer

FIG. 9. Sample snapshots from individual runs showing the position of particles in the contact layer at time t_{exit} (grey dots). Highlighted are the trajectories (red, green, yellow and blue segments) of four randomly tagged particles with their final location at $t = t_{\text{exit}}$ indicated by a black circle. For the two images marked $t = 100$, all four tagged particles remained within the contact layer at least through that time.

tact layer for longer periods of time before escaping to a subsequent liquid layer. In comparing behavior against different facets for similar parameter values, we note that the [011] case for values ε_{LS} below the structural transition yields terminal times only slightly longer than those for the other two facets. However above the transition, the results in Figs. 10 (b) and (e) show a steep drop in $MSD_c^{\parallel}(t)$ and very short terminal times, which are almost an order of magnitude *smaller* - not larger - than for the other two facets. Therefore, while the planar motion of particles in the contact layer is severely repressed by 2D caged motion, the caged particles escape more rapidly into the third dimension, so to speak, funneling thermal energy toward the colder solid more rapidly.

We recall that under steady state conditions, as in this study, the average density of particles in each liquid layer remains fairly constant, dependent on the local temperature and pressure. On average then, for every particle that leaves the contact layer, another replaces it. At the hotter L/S interface, the caged motion helps funnel hotter more energetic particles to the next liquid layer along the $+\hat{z}$ axis, which is cooler. At the colder L/S interface, the caged motion helps funnel colder less energetic particles to the next liquid layer along the $-\hat{z}$ axis, which is warmer. These particles are rapidly replaced by hotter

particles from the warmer layer, which then transfer energy to the first crystalline layer. In either case, the 2D caging motion against the [011] facet enhances thermal transfer near the interface when compared to the other two facets.

The 2D caged motion against the [011] facet we have described is unlike the 3D caged motion observed in equilibrium simulations of glass-forming liquids. Glassy dynamics has been studied in simple hard sphere models as the concentration approaches approaches the critical packing fraction [57] and in binary mixtures of LJ particles upon approach to the vitrification temperature [58]. Three dimensional caged motion is known to occur in complex fluids such as water, molten silicon, polymers and long chain biological molecules, in part due to more complex intermolecular potentials which are orientation dependent. The formation of a plateau-like region in the 3D mean square displacement signaling 3D caging is normally attributed to two effects. Not only are individual particles trapped in cages formed by neighboring particles, but those neighbors are also situated within other cages, thereby causing a significant slowing in the overall motion [59]. In such systems, the colder the temperature and the stronger the particle interaction energy, the stronger the 3D dynamic cage and the longer the confine-
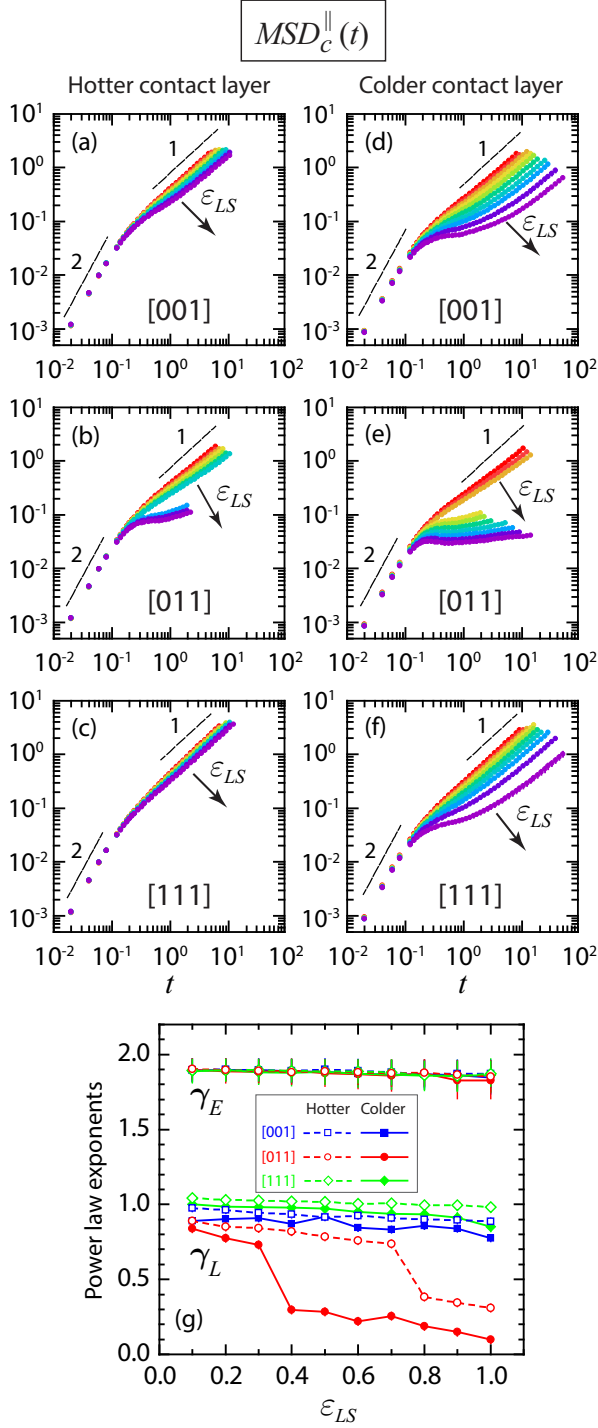
FIG. 10. (a)-(f) Mean square displacement $MSD_c^{\parallel}(t)$ given by Eq. (11) for three facets and $0.1 \leq \varepsilon_{LS} \leq 1.0$ in increments of 0.1. The data shown is restricted to trajectories of particles ten or more of which remain within contact layer throughout entire measurement interval. Superposed lines denote exponent values for ideal ballistic (γ_E) and ideal diffusive (γ_L) motion. Vertical lines through icons signify standard deviation. (g) Exponents extracted from least squares fit to data in (a)-(f); connecting segments are a guide to the eye.

ment time before re-escape and re-trapping by another cage. By contrast in our system, the colder the temperature and the stronger the L/S interaction energy, the stronger the 2D dynamic cage but the shorter the confinement time and the more rapid the escape to the adjacent liquid layer.
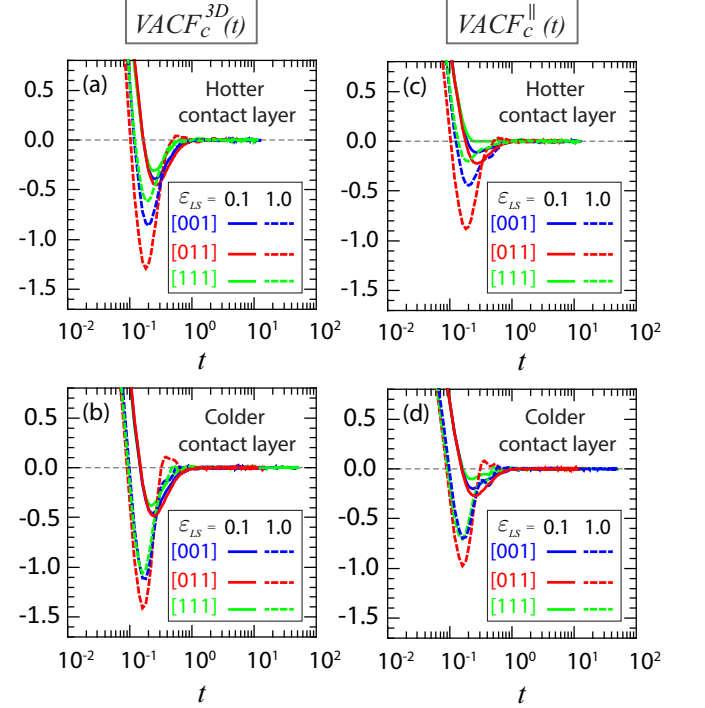

FIG. 11. Velocity autocorrelation function $VACF_c(t)$ given by Eq. (13) for three facets and $\varepsilon_{LS} = 0.1$ and 1.0 for trajectories of particles ten or more of which remain within the contact layer throughout the measurement interval. Superscripts $3D$ and $\parallel$ denote evaluation of Eq. (13) based either on $3D$ or in-plane 2D velocity vectors, respectively.

2. 2D and 3D velocity autocorrelation function of particles which never leave the contact layer

Caged motion can also be inferred from the velocity autocorrelation function. Early simulations of fluids in equilibrium modeled as LJ particles interacting via a soft repulsive potential like $U(r) = \varepsilon_{LL}(\sigma/r)^{15}$ showed that upon approach to vitrification, there develops a period of negative velocity autocorrelation immediately following the early ballistic regime [60, 61]. This behavior has been attributed to the reversed motion of a particle undergoing collisions with neighboring particles which encircle it by a temporary mobile cage; the inclusion of attractive forces enhances the cohesiveness or strength of the cage thereby prolonging the period of transient confinement.

Transient negative autocorrelation is also seen in Fig. 11 showing the results for $VACF_c^{3D}(t)$ and $VACF_c^{\parallel}(t)$. Comparing the time intervals here with the 2D mean

square displacement in Fig. 10, it appears that the start of the negative autocorrelation coincides with the end of the sub-ballistic regime and onset of 2D caged regime. As expected, the amplitude of the negative autocorrelation is larger for particles inside a colder contact layer due to the reduction in particle kinetic energy. Contrasting the behavior for $\varepsilon_{LS} = 0.1\, and\, 1.0$ shows a more pronounced oscillatory behavior about zero upon escape from a transient 2D cage; these oscillations are related to stronger memory effects associated with stronger influence from the periodic crystal surface potential. The results also indicate a there is a stronger dependence on facet orientation and layer temperature for $\varepsilon_{LS} = 1.0$ than $\varepsilon_{LS} = 0.1$, again highlighting the influence of the periodic surface potential on nearby liquid motion. The special character of motion within a contact layer against the [011] facet is again evident. For the same value ε_{LS} and similar layer temperature, the [011] facet induces the *strongest* yet *shortest* period of localization due to 2D caging quantified by the larger amplitude but shorter period of negative velocity autocorrelation. For all parameter values tested, the velocity autocorrelation function was found to decay to zero beyond $t \gtrsim 1.0$. The results indicate that the caging effect is strongest for the [011] case and weakest for the [111] case.

The liquid behavior against the [011] facet exhibits another key feature most easily seen in Fig. 11 for $\varepsilon_{LS} = 1.0$. Following the negative autocorrelation period in $VACF_c^{3D}(t)$ or $VACF_c^{\parallel}(t)$, only the [011] case gives rise to subsequent positive values. Furthermore, the average time spent confined within a dynamic cage, as measured from the time interval between zero crossing points for transient trapping and escape, is shortest for particles in the colder - not hotter - layer, a seemingly counter-intuitive result. As discussed previously in evaluating the results of Figs. 10 (b) and (e), for values of ε_{LS} above the structural transition in the contact layer, particles adjacent to the [011] facet escape more rapidly. As confirmed too by the results in Fig. 11 for the [011] case as well, despite that such particles experience stronger 2D caged motion and therefore smaller 2D mean square displacements, caged particles escape more rapidly into the third dimension i.e. subsequent liquid layers.

Finally, while the curves for $VACF_c^{3D}(t)$ and $VACF_c^{\parallel}(t)$ appear generally similar, there is an important distinction worth noting. Comparison of the amplitude for the negative autocorrelation between the three facets and different layer temperatures for $\varepsilon_{LS} = 1.0$ reveals that the dominant contribution to the results shown stems from 2D motion within the contact layer. This is also true for $\varepsilon_{LS} = 0.1$ although the effect is less pronounced due to less of an influence from the periodic solid surface potential. This suggests that irrespective of layer temperature and facet orientation, most of the time spent in caged motion is caused by repeated transient trapping and escape while confined to the contact layer and less so from confinement effects in the out-of-plane direction ($\hat{z}$ axis) caused by the liquid layering in

Fig. 3.

3. 2D self-intermediate scattering function of particles which never leave the contact layer

The strength of caged motion is typically quantified by the 2D self-intermediate scattering function (SISF) $F_c^{\parallel}(\vec{k}_o, t)$ defined in Eq. (12), where $\vec{k}_o$ is the wave vector corresponding to the first peak in the structure factor. The results in Fig. 12 show that only for a small parameter set and only for the [111] case does the motion undergo a direct transition from ballistic-like to diffusive-like dynamics. The trajectories of particles in those contact layers are therefore the most liquid-like. All other curves in Fig. 12 exhibit some degree of caged motion terminating at a non-zero value, without subsequent diffusive-like decay. For large ε_{LS}, the colder [111] facet induces an unusual signature as well marked by a lengthy interval of negative constant slope, behavior not seen in 3D glassy systems either. Re-inspection of the 2D radial distribution in Fig. 6, 2D structure factor in Fig. 7 and snapshots in Fig. 9 indicate that the negative slope is likely due to the formation of an epitaxial contact layer.

In conventional glassy systems undergoing caged motion, the 3D counterpart of Eq. (12) exhibits three distinct regimes: early ballistic, intermediate caging (plateau) and late time diffusion. Numerous studies have shown that in many 3D glassy systems, the SISF from early to late times can be fit by a double stretched exponential, each term represented by the Kohlrausch-Williams-Watt function. The onset of the plateau signals the transition from ergodic to non-ergodic behavior; for this reason, the amplitude of the plateau region is called the non-ergodicity parameter [58, 62, 63]. This fitting function remains ever popular since the extracted time constants provide estimates of the average relaxation times associated with early ballistic and late time diffusive motion.

In the system under study, however, with the exception of the [111] facet for small ε_{LS}, the majority of curves in Fig. 12 cannot be fit by the usual double exponential function since they do not asymptote to zero despite that the measurement interval extends three to four decades in time. Instead, the curves terminate at a non-zero value, whose magnitude depends on ε_{LS}, facet and temperature. Generally, it appears that the colder the layer temperature or the larger the value ε_{LS}, the more prolonged the plateau-like region and the larger the value F^*).

The influence of facet orientation highlights some special features of the [011] case. The curves in Fig. 12 (b) and (e) are well separated by a large gap due to the structural transition described earlier in Fig. 8 and Fig. 10(g). The two sets of curves exhibit different character. For smaller values ε_{LS}, the curves look like typical 3D SISF curves describing unhindered motion in a homogeneous isotropic fluid except that the diffusive tail
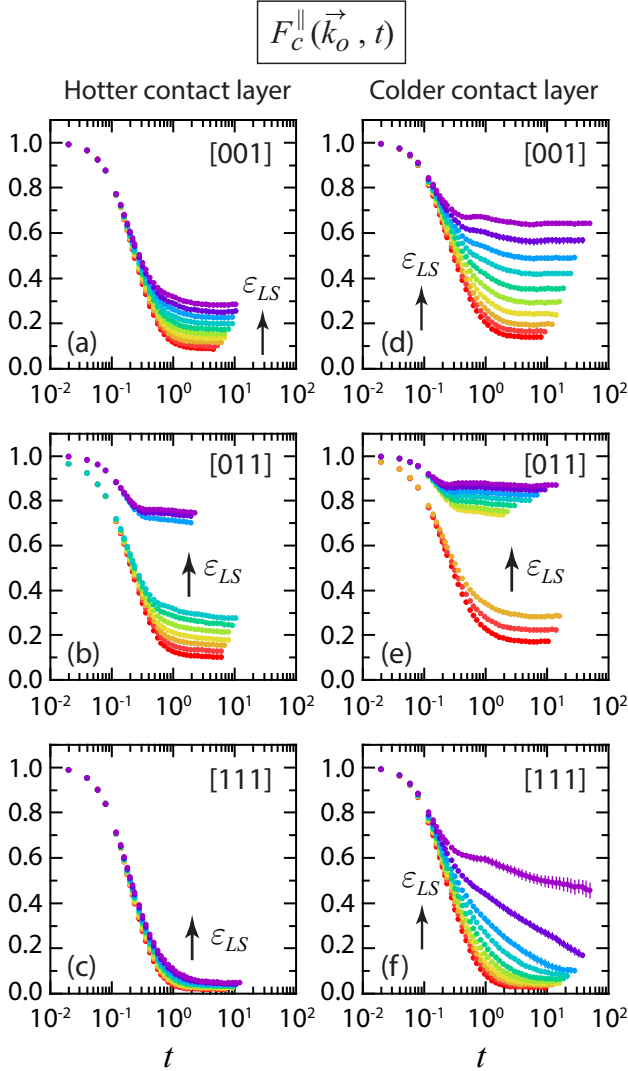
FIG. 12. (a)-(f) Self-intermediate scattering function $F_c^{\parallel}(\vec{k}_o, t)$ given by Eq. (12) for three facets and $0.1 \leq \varepsilon_{LS} \leq 1.0$ in increments of 0.1 for trajectories of particles ten or more of which remain within contact layer throughout the measurement interval. Wave number coordinates of the reciprocal lattice vectors corresponding to the maxima of the 2D static in-plane structure factor are listed in Table III. Vertical lines through icons signify standard deviation (not visible when smaller than icon size).

never decays to zero. The non-zero asymptotic value of the SISF below the structural transition implies persistent autocorrelation while undergoing diffusion caused by influence of the periodic corrugation of the crystal surface potential. Above the transition, the SISF curves in Fig. 12 (b) and (e) instead reveal a rather flat distinctive plateau, indicative of strong caged motion. In comparing motion against the three facets, we see that for the same value of ε_{LS}, the [011] facet induces the strongest degree of caging but surprisingly, the shortest period of confinement. The latter confirms faster escape of particles from

the contact layer to the subsequent liquid layer.

4. Dependence of non-ergodicity parameter on crystal facet, L/S interaction energy and temperature

The dependence of the terminal time t^* and non-ergodicity parameter value F^* as ε_{LS} increases is shown in Fig. 13. When combined with the findings in Fig. 10, the results in Fig. 13(a) highlight that above the value ε_{LS} relating to the structural transition for the [011] case, particles spend the least amount of time undergoing 2D caged motion than similarly parameterized motion for contact layers against the [001] or [111] facet. The caging residence time is much therefore shorter despite that the caging is stronger as quantified by the value F^* in Fig. 13(b). Below the structural transition, for the same value ε_{LS}, liquid particles against the [011] facet spend similar or slightly longer times undergoing sub-diffusive or weakly caged motion as particles against the other two facets. However, for similar contact layer temperature and identical value ε_{LS}, the [011] case always incurs the largest value of F^*. As described in Section II C, data collection was terminated at time t^* once there were fewer than 10 particles that had never left the contact layer. A different criterion for minimum residency will of course yield different values of t^* and F^* but the trends described should still distinguish the [011] facet from the other two.

IV. DISCUSSION

The early NEMD studies cited in the Introduction as well as more recent continuum [64–66] and particle based simulations [21, 22, 29–31, 33, 67–72] all confirm that an enhancement in L/S wettability or increase in liquid pressure generally leads to a reduction in the thermal boundary resistance and thermal slip length at a L/S interface. This correspondence has been attributed to the higher resulting contact density from enhanced liquid on solid adsorption/absorption and/or a smaller depletion layer. Intuitively, it seems reasonable that a higher contact density will promote more frequent collisions between liquid and solid particles thereby enhancing the rate at which thermal energy is transferred across the interface. While the results in Fig. 5(a) confirm that all things equal, larger values of ε_{LS} lead to smaller thermal slip lengths, the data in Fig. 5(b) highlight a contradiction of sorts with this prevailing view. Specifically, for the same value ε_{LS}, the [011] facet supports the highest thermal flux yet maintains the smallest contact density of all three facets tested. From this demonstration alone, it is clear that a single variable like ρ_c cannot reliably nor uniquely predict the relative magnitude in thermal slip length. This counterexample motivated the current study in which various metrics relating to the structural and dynamic properties of particle motion in the contact layer are used to piece
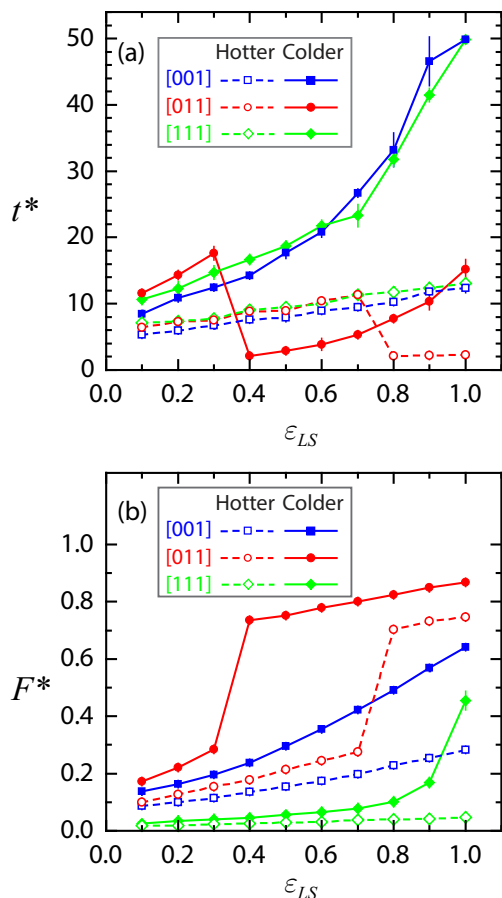
FIG. 13. (a) Terminal time t^* and (b) corresponding value of the self-intermediate scattering function F^* extracted from data in Fig. 12 for the hotter and colder contact layer for three facets and $0.1 \leq \varepsilon_{LS} \leq 1.0$ in increments of 0.1. Vertical lines through icons represent standard deviation; connecting segments are a guide to the eye.

together a more accurate picture of how thermal energy is best transferred across the interfacial region. By confining the liquid layer between two solids, each oriented identically along one of three facets of an FCC crystal, it becomes clearer how the different facet symmetry, width and depth of the periodic crystal surface potential and local temperature influences the configuration and motion of particles in the contact layer. The two L/S interfaces, one at the hotter and colder side of the liquid layer, act essentially as phonon filters which regulate the maximum rate of heat transfer across the entire system. Quantification of particle trajectories by mean square displacement and the self-intermediate scattering function reveals that a smaller thermal slip length is strongly correlated with more rapid particle escape from 2D caged motion in the contact layer. And the stronger the caging effect, the smaller the thermal slip length. As has been noted for supercooled liquids and so-called structural glasses [73], it is highly likely that in our system too, as a particle escapes one cage and gets trapped by a next, it does not do

so alone since its displacement causes coherent motion of neighboring particles as well. The type of 2D caged motion described in this work likely pertains more broadly to the coherent motion of clusters of neighboring particles and therefore sub-diffusive behavior characterized by a much larger effective mass. Besides the retarding influence of the periodic crystal surface potential, this effect too may help explain the reduction in the exponent values γ_L in Table IX.

We end this discussion with an explanation for why our findings stand in sharp contrast to the main conclusion of a previous study which remains highly cited to this day [74]. The authors of that work reported no discernible effect on thermal transfer across the L/S interface which could be traced to the degree of in-plane liquid ordering for a net thermal gradient in the direction parallel or perpendicular to the contact layer. This conclusion was based on the observation that the thermal distribution, thermal gradient and thermal conductivity of the liquid layer remained unchanged despite varying the liquid layer thickness and increasing ε_{LS} from 0.2 to 3.3. Closer inspection of the data in that study suggests three important factors that were overlooked. First, the value $\varepsilon_{LS} = 3.3$ selected to represent a strongly wetting liquid was so large as to induce epitaxial locking of the contact layer to the solid surface for all cases tested. This problem is evident in Fig. 3 of Ref. [74] showing perfect registry between the particles in the contact layer and the pattern set by the periodic surface potential describing the [100] facet of an FCC crystal. This behavior would not only significantly repress 2D diffusive motion within the contact layer by would also create a solid-like interstitial layer. Secondly, the density and temperature of the liquid layer were chosen to be too close to the triple point [36] thereby also incurring formation of solid-like domains within the contact layer. Thirdly, the thickness of the solid layers abutting the liquid layer were reported to be 10× the edge length of the FCC unit cell. The thickness of the solid layers was therefore less than the phonon mean free path [22, 38, 44], which would restrict the set of vibrational frequencies able to couple to the liquid layer.

V. CONCLUSION

The results of this study reveal that a reduction in thermal slip length at a L/S interface is highly correlated with two mechanisms acting in concert. The first is based on strong commensurability between the long range spatial ordering of liquid particles in the contact layer and the spatial pattern describing the periodic surface potential of the nearby crystalline solid. Strong registration between these two patterns establishes higher and more strongly correlated energy barriers the induce a significant slowdown in the 2D mean square displacement following the ballistic regime leading to a new type of 2D caged motion that differs from conventional glassy behav-

ior. Results of the self-intermediate scattering function confirm that smaller thermal slip lengths correlate positively with larger values of the non-ergodicity parameter. Surprisingly, however, larger values of this parameter correspond to shorter - not longer - caging times. It appears then that the stronger the 2D caging effect, the more rapidly caged particles escape into the third dimension so to speak, and in so doing, tunnel between liquid layers to shuttle heat more efficiently toward cooler regions. The fundamental nature of this study suggests broader applicability with a new paradigm for the design of L/S interfaces to maximize thermal transport.

ACKNOWLEDGMENTS

[1] W. M. Deen, *Analysis of Transport Phenomena*, 2nd ed. (Oxford Univ. Press, Inc., New York, NY, 2012).

[2] P. L. Kapitza, Heat transfer and superfluidity of helium II, Phys. Rev. **60**, 354 (1941).

[3] L. L. Liou, B. Bayraktaroglu, and C. I. Huang, Theoretical thermal runaway analysis of heterojunction bipolar transistors: Junction temperature rise threshold, Solid–State Electron. **39**, 165 (1996).

[4] D. B. Tuckerman and R. F. W. Pease, High-performance heat sinking for VLSI, IEEE Electron Device Lett. **2**, 126 (1981).

[5] E. T. Swartz and R. O. Pohl, Thermal boundary resistance, Rev. Mod. Phys. **61**, 605 (1989).

[6] E. T. Swartz and R. O. Pohl, Thermal resistance at interfaces, Appl. Phys. Lett. **51**, 2200 (1987).

[7] D. Bolmatov, V. V. Brazhkin, and T. K., The phonon theory of liquid thermodynamics, Sci. Rep. **2** (2012).

[8] R. J. Warzoha, A. A. Wilson, B. F. Donovan, A. Clark, X. Cheng, L. An, E. Lee, X. Liu, and G. Feng, Confined transducer geometries to enhance sensitivity to thermal boundary conductance in frequency–domain thermoreflectance measurements, in *ASME 2021 International Technical Conference and Exhibition on Packaging and Integration of Electronic and Photonic Microsystems* (ASME, Virtual, 2021) pp. IPACK2021–66842.

[9] K. Yu, R. Enright, and D. McCloskey, Quantifying interfacial thermal conductance at solid–liquid interfaces using frequency-domain thermoreflectance and analytical methods, in *21st IEEE Intersociety Conference on Thermal and Thermomechanical Phenomena in Electronic Systems (iTherm)* (IEEE, San Diego, CA, 2022) pp. 1–6.

[10] E. Helfand and S. A. Rice, Principle of corresponding states for transport properties, J. Chem. Phys. **32**, 1642 (2016).

[11] A. Tenenbaum, G. Ciccotti, and R. Gallico, Stationary nonequilibrium states by molecular dynamics. Fourier's law, Phys. Rev. A **25**, 2778 (1982).

[12] S. A. Somers and H. T. Davis, Microscopic dynamics of fluids confined between smooth and atomically structured solid surfaces, J. Chem. Phys. **96**, 5389 (1992).

[13] J. R. Henderson and F. van Swol, On the interface between a fluid and a planar wall: Theory and simulations of a hard sphere fluid at a hard wall, Mol. Phys. **51**, 991 (1984).

[14] J. Gao, W. D. Luedtke, and U. Landman, Layering transitions and dynamics of confined liquid films, Phys. Rev. Lett. **79**, 705 (1997).

[15] S. Matsumoto, Molecular dynamics simulation of a liquid droplet on a solid surface, J. Jap. Soc. Tribologists **42**, 93 (1997).

[16] S. Maruyama and T. Kimura, Liquid droplet in contact with a solid surface, Micro. Thermophys. Eng. **2**, 49 (1998).

[17] S. Maruyama and T. Kimura, Intermolecular energy transfer at a solid–liquid interface, Micro. Thermophys. Eng. **4**, 189 (2000).

[18] J.-L. Barrat and F. Chiaruttini, Kapitza resistance at the liquid–solid interface, Mol. Phys. **101**, 1605 (2003).

[19] L. Xue, P. Keblinski, S. R. Phillpot, S. U.-S. Choi, and J. A. Eastman, Two regimes of thermal resistance at a liquid–solid interface, J. Chem. Phys. **118**, 337 (2003).

[20] M. Vuorio, Role of wetting and nanoscale roughness on thermal conductance at liquid–solid interface, Appl. Phys. Lett. **99**, 073112 (2011).

[21] S. Murad and I. K. Puri, Thermal transport across nanoscale solid–fluid interfaces, Appl. Phys. Lett. **92**, 133105 (2008).

[22] H. Han, S. Mérabia, and F. Müller-Plathe, Thermal transport at solid–liquid interfaces: High pressure facilitates heat flow through nonlocal liquid structuring, J. Phys. Chem. Lett. **8**, 1946 (2017).

[23] G. Balasubramanian, S. Banerjee, and I. K. Puri, Unsteady nanoscale thermal transport across a solid–fluid interface, J. Appl. Phys. **104**, 064306 (2008).

[24] A. K. M. M. Morshed, T. Paul, and J. A. Khan, Atomistic simulation of temperature dependent thermal transport across nanoconfined liquid, Physica E **47**, 246 (2013).

[25] T. Ohara and D. Torii, Molecular dynamics study of thermal phenomena in an ultrathin liquid film sheared between solid surfaces: The influence of the crystal plane on energy and momentum transfer at solid-liquid interfaces, J. Chem. Phys. **122**, 214717 (2005).

[26] D. Torii, T. Ohara, and K. Ishida, Molecular-scale mechanism of thermal resistance at the solid–liquid interfaces: Influence of interaction parameters between solid and liquid molecules, J. Heat Transfer **132**, 012402 (2010).

[27] B. H. Kim, A. Beskok, and T. Cagin, Molecular dynamics simulations of thermal resistance at the liquid-solid interface, J. Chem. Phys. **129**, 174701 (2008).

[28] S. Maruyama and T. Kimura, A study on thermal resistance over a solid–liquid interface by the molecular dynamics method, Thermal Sci. Eng. **7**, 63 (1999).

[29] S. Murad and I. K. Puri, Molecular simulation of thermal transport across hydrophilic interfaces, Chem. Phys. Lett. **467**, 110 (2008).

[30] A. Pham, M. Barisik, and B. Kim, Pressure dependence of Kapitza resistance at gold/water and silicon/water interfaces, J. Chem. Phys. **139**, 244702 (2013).

[31] S. Ge and M. Chen, Temperature dependence of thermal resistance at a solid/liquid interface, Mol. Phys. **111**, 903 (2013).

[32] S. W. Hung, G. Kikugawa, and J. Shiomi, Mechanism of temperature dependent thermal transport across the interface between self-assembled monolayer and water, J. Phys. Chem. C **120**, 26678 (2016).

[33] B. Ramos-Alvarado, S. Kumar, and G. P. Peterson, Solid–liquid thermal transport and its relationship with wettability and the interfacial liquid structure, J. Phys. Chem. Lett. **7**, 3497 (2016).

[34] A. Michels, H. Wijker, and H. Wijker, Isotherms of argon between 0°C and 150°C and pressures up to 2900 atmospheres, Physica **XV**, 627 (1949).

[35] L. Verlet, Computer "experiments" on classical fluids. i. Thermodynamical properties of Lennard-Jones molecules, Phys. Rev. **159**, 98 (1967).

[36] B. L. Holian and D. J. Evans, Shear viscosities away from the melting line: A comparison of equilibrium and nonequilibrium molecular dynamics, J. Chem. Phys. **78**, 5147 (1983).

[37] M. Thol, G. Rutkai, A. Köster, R. Lustig, R. Span, and J. Vrabec, Equation of state for the Lennard-Jones fluid, J. Phys. Chem. Ref. Data **45**, 023101 (2016).

[38] R. J. Stevens, L. V. Zhigilei, and P. M. Norris, Effects of temperature and disorder on thermal boundary conductance at solid–solid interfaces: Nonequilibrium molecular dynamics simulations, Int. J. Mech. Sci. **50**, 3977 (2007).

[39] C. S. Barrett and L. Meyer, X–ray diffraction of solid argon, J. Chem. Phys. **41**, 1078 (1964).

[40] S. Plimpton, Fast parallel algorithms for short–range molecular dynamics, J. Comput. Phys. **117**, 1 (1995).

[41] A. P. Thompson, H. M. Aktulga, R. Berger, D. S. Bolintineanu, W. M. Brown, P. S. Crozier, P. J. intVelde, A. Kohlmeyer, S. G. Moore, T. D. Nguyen, R. Shan, M. J. Stevens, J. Tranchida, C. Trott, and S. J. Plimpton, LAMMPS – A flexible simulation tool for particle–based materials modeling at the atomic, meso, and continuum scales, Comp. Phys. Comm. **271**, 108171 (2022).

[42] W. G. Hoover, Canonical dynamics: Equilibrium phase–space distributions, Phys. Rev. A **31**, 1695 (1985).

[43] T. Schneider and E. Stoll, Molecular–dynamics study of a three–dimensional one–component model for distortive phase transitions, Phys. Rev. B **17**, 1302 (1978).

[44] Z. Liang and P. Keblinski, Finite–size effects on molecular dynamics interfacial thermal–resistance predictions, Phys. Rev. B **90**, 075411 (2014).

[45] In studies of liquid systems, the structure factor is often computed from the relation $|\sum_i^{N_c} \exp(-i\boldsymbol{k} \cdot \boldsymbol{r}_i)|^2$ instead of Eq. (10). The quadratic relation, however, is only strictly valid for liquid particles situated on the sites of a Bravais lattice.

[46] S. Toxvaerd, The structure and thermodynamics of a solid–fluid interface, J. Chem. Phys. **74**, 1998 (1981).

[47] E. Velasco and P. Tarazona, Phase transitions at solid–fluid interfaces: Theoretical description of the transverse structure, Surf. Sci. **251/252**, 628 (1991).

[48] P. A. Thompson and M. O. Robbins, Shear flow near solids: Epitaxial rrder and flow boundary conditions, Phys. Rev. A **41**, 6830 (1990).

[49] B. D. Todd and D. J. Evans, The heat flux vector for highly inhomogeneous nonequilibrium fluids in very narrow pores, J. Chem. Phys. **103**, 9804 (1995).

[50] N. V. Priezjev, A. A. Darhuber, and S. M. Troian, Slip behavior in liquid films on surfaces of patterned wettability: Comparison between continuum and molecular dynamics, Phys. Rev. E **71**, 041608 (2005).

[51] M. Barisik and A. Beskok, Temperature dependence of thermal resistance at the water/silicon interface, Int. J. Therm. Sci **77**, 47 (2014).

[52] G. L. Pollack, Kapitza resistance, Rev. Mod. Phys. **41**, 48 (1969).

[53] I. M. Khalatnikov, *An Introduction to the Theory of Superfludity*, CRC Press (Taylor & Francis, Boca Raton, FL, 2018) english translation of Russian edition by P. C. Hohenberg.

[54] P. Langevin, Sur la théorie du mouvement Brownien, C.R. Acad. Sci. Paris **146**, 530 (1908).

[55] V. Vladimirsky and Y. A. Terletzky, Hydrodynamical theory of translational Brownian motion, Zh. Eksp. Teor. Fiz. **15**, 258 (1945).

[56] E. J. Hinch, Application of the Langevin equation to fluid suspensions, J. Fluid Mech. **72**, 495 (1975).

[57] M. Fuchs, W. Götze, and M. R. Mayr, Asymptotic laws for tagged-particle motion in glassy systems, Phys. Rev. E **58**, 3384 (1998).

[58] W. Kob and H. C. Andersen, Scaling behavior in the β–relaxation regime of a supercooled Lennard-Jones mixture, Phys. Rev. Lett. **73**, 1376 (1994).

[59] W. Kob, Computer simulations of supercooled liquids and glasses, J. Phys.: Condens. Matter **11**, R85 (1999).

[60] D. P. Dean and J. N. Kushick, On the role of attractive forces in the cage effect in simple liquids, J. Chem. Phys. **76**, 619 (1982).

[61] Y. Endo and E. H., Microscopic mechanism of the cage effect in simple liquids, Phys. Lett. **95A**, 92 (1983).

[62] G. Wahnström, Molecular–dynamics study of a supercooled two-component Lennard–Jones system, Phys. Rev. A **44**, 3752 (1991).

[63] R. D. Mountain and D. Thirumalai, Relationship between the fluctuation metric and the non-ergodicity parameter: incoherent scattering function, Physica A **192**, 543 (1993).

[64] R. S. Prakash, Surface chemistry and characteristics based model for the thermal contact resistance of fluidic interstitial thermal interface materials, ASME **123**, 969 (2001).

[65] A. Hamasaiid, M. Dargusch, T. Loulou, and G. Dour, A predictive model for the thermal contact resistance at liquid–solid interfaces: Analytical developments and validation, Int. J. Therm. Sci **50**, 1445 (2011).

[66] S. Y. Misyura, Dependence of wettability of microtextured wall on the heat and mass transfer: Simple estimates for convection and heat transfer, Int. J. Therm. Sci **170**, 105353 (2020).

[67] N. Shenogina, R. Godawat, P. Keblinski, and S. Garde, How wetting and adhesion affect thermal conductance of a range of hydrophobic to hydrophilic aqueous interfaces, Phys. Rev. Lett. **102**, 156101 (2009).

[68] M. Han, Effect of liquid bulk density on thermal resistance at a liquid–solid interface, J. Mech. Sci. Tech **25**,

37 (2011).

[69] M. Shibahara and K. Takeuchi, A molecular dynamics study on the effects of nanostructural clearances on thermal resistance at a Lennard-Jones liquid-solid interface, J. Thermal Sci. Tech. , 9 (2011).

[70] J. Zhang, F. Leroy, and F. Müller-Plathe, Evaporation of nanodroplets on heated substrates: A molecular dynamics simulation study, Langmuir **29**, 9770 (2013).

[71] M. E. Caplan, A. Giri, and P. E. Hopkins, Analytical model for the effects of wetting on thermal boundary conductance across solid/classical liquid interfaces, J. Chem. Phys. **140**, 154701 (2014).

[72] S. Alosious, S. K. Kannam, S. P. Sethian, and B. D. Todd, Prediction of Kapitza resistance at fluid–solid interfaces, J. Chem. Phys. **151**, 194502 (2019).

[73] V. Lubchenko and P. G. Wolynes, Theory of structural glasses and supercooled liquids, Annu. Rev. Phys. Chem **58**, 235 (2007).

[74] L. Xue, P. Keblinski, S. R. Phillpot, S. U.-S. Choi, and J. A. Eastman, Effect of liquid layering at the liquid–solid interface on thermal transport, Int. J. Mech. Sci. **47**, 4277 (2004).

TABLE VII. Results of NEMD simulations described in the text for $T_{\text{source}} = 1.6$ and $T_{\text{sink}} = 1.0$ showing the influence of FCC facet orientation and L/S interaction energy ε_{LS} on the thermal flux J_z [Eq. (8)] and magnitude of the thermal gradient $|dT/dz|$ and thermal conductivity k [Eq. (2)] within the bulk solid and liquid layers away from the L/S interface. The numerical values in each column are to be multiplied by the multiplicative factor appearing in the column heading. Thermal gradient values were extracted from least squares fits across the linear portion of the thermal profile within each layer. Numbers in parentheses are standard deviation values. All values are reported in reduced units.

Facet	ε_{LS}	$J_z \times 10^{-2}$	Liquid layer			Hotter solid layer		Colder solid layer	
			$|dT/dz| \times 10^{-2}$	k		$|dT/dz| \times 10^{-4}$	$k \times 10^{2}$	$|dT/dz| \times 10^{-4}$	$k \times 10^{2}$
[001]	0.1	6.861(0.067)	0.903(0.029)	7.607(0.257)		3.400(1.630)	2.352(0.911)	2.800(1.180)	3.087(1.949)
[001]	0.2	7.297(0.089)	0.983(0.027)	7.429(0.240)		3.990(2.180)	3.844(5.758)	3.370(0.940)	2.370(0.846)
[001]	0.3	8.045(0.364)	1.042(0.030)	7.725(0.422)		4.350(2.170)	3.315(3.577)	3.120(1.670)	3.372(1.830)
[001]	0.4	8.280(0.084)	1.102(0.028)	7.520(0.208)		5.110(1.930)	1.886(0.831)	3.640(1.460)	2.784(1.571)
[001]	0.5	8.661(0.088)	1.161(0.017)	7.464(0.112)		4.590(1.860)	2.840(2.848)	4.040(1.100)	2.379(0.991)
[001]	0.6	8.609(0.576)	1.191(0.026)	7.230(0.485)		5.050(1.360)	1.825(0.513)	3.730(1.020)	2.461(0.667)
[001]	0.7	9.297(0.095)	1.227(0.022)	7.581(0.088)		6.750(1.810)	1.478(0.429)	4.090(0.840)	2.379(0.601)
[001]	0.8	9.580(0.327)	1.294(0.020)	7.408(0.308)		5.250(1.670)	2.111(1.107)	3.470(1.320)	4.277(5.245)
[001]	0.9	9.702(0.035)	1.316(0.027)	7.375(0.145)		5.940(1.730)	1.775(0.562)	3.890(1.250)	2.755(0.937)
[001]	1.0	9.924(0.375)	1.355(0.025)	7.325(0.251)		5.340(2.210)	2.126(0.758)	3.930(0.930)	2.663(0.686)
[011]	0.1	7.677(0.103)	1.043(0.018)	7.366(0.149)		4.110(1.790)	4.934(9.810)	3.380(0.870)	2.410(0.603)
[011]	0.2	8.355(0.196)	1.098(0.020)	7.615(0.272)		4.770(1.550)	1.949(0.721)	2.980(1.080)	3.243(1.442)
[011]	0.3	8.927(0.053)	1.166(0.025)	7.658(0.150)		5.090(1.150)	1.832(0.393)	2.870(1.380)	3.907(2.281)
[011]	0.4	9.003(0.404)	1.222(0.010)	7.370(0.343)		5.520(1.840)	1.792(0.573)	4.080(0.890)	2.324(0.601)
[011]	0.5	9.566(0.196)	1.279(0.024)	7.484(0.228)		5.790(1.740)	1.802(0.584)	3.250(1.120)	3.402(1.528)
[011]	0.6	10.211(0.638)	1.317(0.017)	7.754(0.425)		5.810(1.440)	1.874(0.543)	3.880(1.080)	2.828(0.803)
[011]	0.7	10.044(0.101)	1.383(0.024)	7.264(0.130)		4.960(1.000)	2.125(0.567)	3.400(1.380)	3.767(2.389)
[011]	0.8	10.303(0.090)	1.406(0.037)	7.333(0.170)		5.010(2.310)	2.674(1.820)	3.230(1.310)	3.878(1.989)
[011]	0.9	10.667(0.120)	1.433(0.026)	7.444(0.180)		5.520(1.320)	2.026(0.437)	3.790(0.990)	3.045(1.003)
[011]	1.0	10.629(0.325)	1.464(0.025)	7.265(0.309)		5.400(1.860)	2.200(0.800)	3.540(0.880)	3.192(0.862)
[111]	0.1	6.975(0.230)	0.914(0.033)	7.639(0.371)		4.010(1.330)	1.985(0.880)	3.270(0.880)	2.328(0.880)
[111]	0.2	7.429(0.148)	0.993(0.031)	7.485(0.138)		3.740(1.650)	2.791(2.486)	3.110(1.040)	2.800(1.481)
[111]	0.3	8.017(0.397)	1.059(0.026)	7.572(0.391)		4.190(1.730)	2.318(1.146)	2.830(1.050)	3.316(1.586)
[111]	0.4	8.477(0.189)	1.131(0.014)	7.493(0.131)		4.440(1.460)	2.201(1.063)	3.440(1.160)	2.765(1.102)
[111]	0.5	8.909(0.097)	1.179(0.024)	7.559(0.121)		5.340(2.170)	2.010(0.990)	3.440(0.880)	2.763(0.763)
[111]	0.6	9.318(0.061)	1.231(0.029)	7.574(0.185)		5.830(0.930)	1.638(0.285)	2.870(1.720)	8.488(13.281)
[111]	0.7	9.608(0.128)	1.280(0.020)	7.508(0.179)		5.150(1.380)	2.021(0.671)	3.400(1.130)	3.216(1.395)
[111]	0.8	10.003(0.115)	1.335(0.018)	7.496(0.144)		4.830(1.540)	2.289(0.799)	3.530(1.300)	3.577(2.368)
[111]	0.9	10.207(0.062)	1.362(0.020)	7.495(0.097)		5.660(1.440)	1.918(0.525)	3.710(1.680)	3.493(2.071)
[111]	1.0	10.394(0.061)	1.403(0.017)	7.408(0.113)		5.150(2.640)	3.526(4.032)	3.710(1.350)	3.385(1.891)

TABLE VIII. Results of NEMD simulations described in the text for $T_{source} = 1.6$ and $T_{sink} = 1.0$ showing the influence of FCC facet orientation and L/S interaction energy ε_{LS} on contact layer density ρ_c, maximum value of the static in-plane structure factor S_{max} [Eq. (10)], contact layer temperature T_c [Eq. (7)], thermal jump ΔT and thermal slip length L_T [Eq. (3)]. Numbers in parentheses are standard deviation values. All values are reported in reduced units.

| Facet | ε_{LS} | Hotter contact layer | | | | | Colder contact layer | | | | |
		ρ_c	S_{max}	T_c	ΔT	L_T	ρ_c	S_{max}	T_c	ΔT	L_T
[001]	0.1	1.351(0.013)	0.083(0.001)	1.451(0.008)	0.139(0.011)	15.457(1.616)	1.567(0.017)	0.124(0.003)	1.168(0.007)	0.155(0.009)	17.172(1.316)
[001]	0.2	1.455(0.029)	0.094(0.001)	1.461(0.007)	0.127(0.010)	12.942(1.279)	1.705(0.037)	0.148(0.002)	1.156(0.004)	0.140(0.006)	14.230(0.730)
[001]	0.3	1.535(0.036)	0.110(0.003)	1.471(0.009)	0.117(0.007)	11.231(0.967)	1.870(0.036)	0.181(0.002)	1.147(0.005)	0.129(0.006)	12.421(0.826)
[001]	0.4	1.629(0.010)	0.125(0.002)	1.475(0.005)	0.110(0.007)	9.975(0.833)	2.007(0.043)	0.222(0.003)	1.137(0.006)	0.116(0.007)	10.519(0.755)
[001]	0.5	1.699(0.024)	0.146(0.002)	1.486(0.006)	0.101(0.005)	8.748(0.568)	2.137(0.019)	0.272(0.004)	1.128(0.005)	0.104(0.003)	8.985(0.311)
[001]	0.6	1.790(0.021)	0.166(0.003)	1.491(0.004)	0.096(0.007)	8.077(0.740)	2.315(0.025)	0.335(0.004)	1.122(0.003)	0.101(0.004)	8.465(0.458)
[001]	0.7	1.869(0.029)	0.189(0.002)	1.492(0.005)	0.091(0.009)	7.461(0.829)	2.521(0.036)	0.403(0.004)	1.110(0.004)	0.089(0.005)	7.281(0.461)
[001]	0.8	1.957(0.030)	0.213(0.001)	1.501(0.004)	0.082(0.005)	6.316(0.488)	2.737(0.033)	0.486(0.004)	1.101(0.003)	0.080(0.005)	6.164(0.473)
[001]	0.9	2.042(0.021)	0.242(0.003)	1.506(0.009)	0.078(0.006)	5.955(0.560)	2.993(0.027)	0.567(0.005)	1.096(0.004)	0.074(0.003)	5.659(0.302)
[001]	1.0	2.126(0.034)	0.274(0.003)	1.513(0.004)	0.073(0.007)	5.362(0.580)	3.269(0.030)	0.645(0.006)	1.089(0.004)	0.069(0.006)	5.101(0.559)
[011]	0.1	0.963(0.021)	0.038(0.001)	1.470(0.006)	0.116(0.006)	11.175(0.607)	0.995(0.023)	0.036(0.001)	1.154(0.004)	0.135(0.007)	12.986(0.790)
[011]	0.2	0.980(0.016)	0.040(0.001)	1.475(0.008)	0.111(0.007)	10.157(0.757)	0.983(0.016)	0.037(0.000)	1.142(0.005)	0.124(0.005)	11.326(0.533)
[011]	0.3	0.970(0.018)	0.043(0.001)	1.484(0.007)	0.101(0.009)	8.697(0.950)	0.941(0.016)	0.040(0.001)	1.131(0.003)	0.113(0.004)	9.685(0.436)
[011]	0.4	0.961(0.017)	0.045(0.001)	1.493(0.003)	0.095(0.004)	7.810(0.354)	1.212(0.031)	0.552(0.002)	1.116(0.004)	0.096(0.003)	7.890(0.249)
[011]	0.5	0.945(0.022)	0.051(0.000)	1.498(0.006)	0.087(0.007)	6.817(0.627)	1.375(0.027)	0.588(0.004)	1.107(0.004)	0.086(0.006)	6.767(0.549)
[011]	0.6	1.006(0.013)	0.055(0.001)	1.506(0.005)	0.077(0.007)	5.860(0.579)	1.549(0.036)	0.651(0.003)	1.099(0.003)	0.082(0.004)	6.251(0.282)
[011]	0.7	1.077(0.027)	0.056(0.001)	1.514(0.004)	0.070(0.006)	5.057(0.493)	1.797(0.023)	0.713(0.003)	1.091(0.003)	0.070(0.004)	5.074(0.376)
[011]	0.8	1.164(0.025)	0.487(0.004)	1.521(0.008)	0.068(0.007)	4.824(0.594)	2.009(0.034)	0.768(0.003)	1.086(0.004)	0.065(0.006)	4.658(0.485)
[011]	0.9	1.253(0.015)	0.554(0.003)	1.526(0.005)	0.064(0.006)	4.485(0.489)	2.237(0.020)	0.814(0.003)	1.079(0.004)	0.058(0.004)	4.047(0.338)
[011]	1.0	1.329(0.013)	0.588(0.004)	1.529(0.006)	0.063(0.005)	4.285(0.378)	2.455(0.038)	0.851(0.003)	1.074(0.004)	0.051(0.005)	3.510(0.359)
[111]	0.1	1.525(0.017)	0.032(0.001)	1.445(0.007)	0.139(0.010)	15.208(1.579)	1.776(0.014)	0.042(0.001)	1.181(0.005)	0.164(0.005)	17.958(0.898)
[111]	0.2	1.664(0.022)	0.035(0.001)	1.452(0.009)	0.134(0.009)	13.498(1.314)	1.988(0.033)	0.048(0.001)	1.165(0.004)	0.145(0.006)	14.661(0.840)
[111]	0.3	1.781(0.026)	0.039(0.001)	1.459(0.008)	0.123(0.007)	11.660(0.878)	2.154(0.024)	0.055(0.002)	1.154(0.004)	0.134(0.006)	12.696(0.742)
[111]	0.4	1.876(0.026)	0.041(0.001)	1.470(0.008)	0.114(0.006)	10.089(0.661)	2.319(0.028)	0.065(0.002)	1.145(0.002)	0.121(0.004)	10.674(0.341)
[111]	0.5	1.989(0.022)	0.045(0.001)	1.475(0.006)	0.109(0.006)	9.260(0.657)	2.505(0.033)	0.076(0.002)	1.132(0.004)	0.110(0.004)	9.317(0.396)
[111]	0.6	2.091(0.027)	0.050(0.001)	1.486(0.006)	0.097(0.008)	7.921(0.745)	2.705(0.028)	0.093(0.002)	1.126(0.007)	0.105(0.005)	8.562(0.505)
[111]	0.7	2.165(0.020)	0.054(0.002)	1.488(0.005)	0.093(0.005)	7.255(0.455)	2.927(0.028)	0.117(0.005)	1.116(0.004)	0.094(0.004)	7.380(0.415)
[111]	0.8	2.260(0.029)	0.059(0.001)	1.498(0.006)	0.086(0.005)	6.418(0.404)	3.171(0.040)	0.159(0.005)	1.110(0.004)	0.086(0.005)	6.455(0.469)
[111]	0.9	2.403(0.018)	0.063(0.001)	1.496(0.005)	0.082(0.003)	6.051(0.315)	3.439(0.035)	0.290(0.033)	1.100(0.004)	0.078(0.004)	5.763(0.374)
[111]	1.0	2.490(0.028)	0.070(0.001)	1.503(0.007)	0.078(0.006)	5.534(0.447)	3.812(0.039)	0.582(0.018)	1.095(0.004)	0.071(0.006)	5.093(0.461)

TABLE IX. Results of NEMD simulations described in the text for $T_{\text{source}} = 1.6$ and $T_{\text{sink}} = 1.0$ showing the influence of FCC facet orientation and L/S interaction energy ε_{LS} on the early (E) time and late (L) time exponent values, γ_E and γ_L respectively, obtained from least square fits to the 2D mean square displacement curves in Fig. 10 (numbers in parentheses are 95% confidence interval values). Also listed are the extracted values of the non-ergodicity parameter $F_c^*(\vec{k}_o)$ [Eq. (12)] at the terminal time τ^* (numbers in parentheses are standard deviation values). All values are reported in reduced units.

Facet	ε_{LS}	Hotter contact layer				Colder contact layer			
		γ_E	γ_L	F^*	t^*	γ_E	γ_L	F^*	t^*
[001]	0.1	1.8969(0.0733)	0.9745(0.0010)	0.0861(0.0047)	5.3100(0.3100)	1.8932(0.0758)	0.8897(0.0022)	0.1375(0.0004)	8.4500(0.5400)
[001]	0.2	1.9017(0.0689)	0.9626(0.0012)	0.0991(0.0029)	5.9400(0.2946)	1.8984(0.0694)	0.9022(0.0018)	0.1631(0.0033)	10.8467(0.5900)
[001]	0.3	1.8952(0.0722)	0.9434(0.0020)	0.1146(0.0006)	6.7100(0.5220)	1.8958(0.0744)	0.9082(0.0018)	0.1953(0.0043)	12.4067(0.3921)
[001]	0.4	1.8899(0.0772)	0.9340(0.0014)	0.1364(0.0004)	7.5800(0.1970)	1.8867(0.0777)	0.8700(0.0024)	0.2379(0.0064)	14.2200(0.1058)
[001]	0.5	1.8990(0.0722)	0.9150(0.0022)	0.1549(0.0010)	7.8700(0.5910)	1.8846(0.0816)	0.9173(0.0020)	0.2959(0.0072)	17.7067(0.8429)
[001]	0.6	1.8912(0.0747)	0.9260(0.0020)	0.1732(0.0025)	8.9600(0.2553)	1.8731(0.0875)	0.8442(0.0020)	0.3542(0.0016)	20.8067(0.7814)
[001]	0.7	1.8801(0.0813)	0.9095(0.0022)	0.1969(0.0044)	9.4800(0.1970)	1.8646(0.0958)	0.8322(0.0024)	0.4213(0.0059)	26.6933(0.6395)
[001]	0.8	1.8700(0.0872)	0.8977(0.0020)	0.2277(0.0026)	10.2800(0.4854)	1.8674(0.0972)	0.8568(0.0020)	0.4901(0.0059)	33.2133(2.5694)
[001]	0.9	1.8727(0.0886)	0.8966(0.0020)	0.2540(0.0018)	11.8200(0.4652)	1.8607(0.1000)	0.8386(0.0020)	0.5681(0.0117)	46.5600(3.6550)
[001]	1.0	1.8715(0.0888)	0.8865(0.0022)	0.2832(0.0063)	12.3267(0.6906)	1.8458(0.1077)	0.7743(0.0025)	0.6410(0.0038)	49.8400(0.0000)
[011]	0.1	1.9025(0.0672)	0.8894(0.0006)	0.0994(0.0036)	6.4300(0.4050)	1.8962(0.0739)	0.8394(0.0016)	0.1713(0.0031)	11.5933(0.5201)
[011]	0.2	1.8963(0.0727)	0.8509(0.0006)	0.1274(0.0016)	7.3133(0.5637)	1.8889(0.0783)	0.7756(0.0016)	0.2216(0.0046)	14.3000(0.7158)
[011]	0.3	1.8894(0.0764)	0.8413(0.0010)	0.1537(0.0019)	7.5133(0.3743)	1.8854(0.0772)	0.7304(0.0014)	0.2846(0.0022)	17.5800(1.0153)
[011]	0.4	1.8826(0.0805)	0.8192(0.0016)	0.1780(0.0034)	8.8333(0.5201)	1.8935(0.0758)	0.2980(0.0062)	0.7358(0.0029)	2.0867(0.1332)
[011]	0.5	1.8870(0.0775)	0.7858(0.0020)	0.2139(0.0060)	8.9067(0.6438)	1.8760(0.0888)	0.2826(0.0030)	0.7520(0.0016)	2.9000(0.5724)
[011]	0.6	1.8810(0.0811)	0.7585(0.0022)	0.2439(0.0051)	10.3733(0.4086)	1.8682(0.0947)	0.2203(0.0032)	0.7783(0.0025)	3.8400(0.9007)
[011]	0.7	1.8760(0.0872)	0.7375(0.0028)	0.2751(0.0043)	11.3133(0.4801)	1.8592(0.1011)	0.2544(0.0028)	0.8010(0.0016)	5.3000(0.1217)
[011]	0.8	1.8769(0.0866)	0.3829(0.0080)	0.7021(0.0022)	2.1067(0.1137)	1.8748(0.0869)	0.1889(0.0006)	0.8242(0.0018)	7.7867(0.3252)
[011]	0.9	1.8654(0.0925)	0.3438(0.0062)	0.7318(0.0023)	2.1933(0.1943)	1.8275(0.1202)	0.1494(0.0014)	0.8488(0.0014)	10.2933(1.1856)
[011]	1.0	1.8536(0.1038)	0.3101(0.0048)	0.7459(0.0030)	2.2500(0.1700)	1.8276(0.1233)	0.0978(0.0016)	0.8679(0.0009)	15.2000(1.4500)
[111]	0.1	1.8930(0.0750)	1.0431(0.0008)	0.0184(0.0039)	7.1500(0.2420)	1.8881(0.0777)	1.0005(0.0004)	0.0249(0.0008)	10.6000(0.4550)
[111]	0.2	1.8953(0.0722)	1.0307(0.0008)	0.0186(0.0024)	7.3667(0.3139)	1.8980(0.0730)	0.9841(0.0004)	0.0347(0.0061)	12.2533(1.0191)
[111]	0.3	1.8960(0.0727)	1.0266(0.0008)	0.0233(0.0006)	7.7900(0.6510)	1.8821(0.0819)	0.9836(0.0006)	0.0391(0.0017)	14.7333(1.0108)
[111]	0.4	1.8923(0.0736)	1.0206(0.0008)	0.0248(0.0006)	9.0500(0.0611)	1.8784(0.0861)	0.9783(0.0008)	0.0449(0.0033)	16.6333(0.1677)
[111]	0.5	1.8870(0.0761)	1.0182(0.0010)	0.0288(0.0010)	9.5100(0.4130)	1.8834(0.0819)	0.9726(0.0006)	0.0555(0.0012)	18.7067(0.5601)
[111]	0.6	1.8876(0.0755)	1.0048(0.0010)	0.0310(0.0012)	9.9667(0.5132)	1.8711(0.0883)	0.9492(0.0008)	0.0648(0.0023)	21.7600(0.8681)
[111]	0.7	1.8806(0.0833)	1.0064(0.0004)	0.0384(0.0018)	11.3667(0.4272)	1.8641(0.0941)	0.9370(0.0010)	0.0783(0.0119)	23.3200(1.6837)
[111]	0.8	1.8619(0.0938)	0.9932(0.0006)	0.0399(0.0040)	11.7467(0.7829)	1.8603(0.1000)	0.9343(0.0010)	0.1011(0.0082)	31.7733(1.0801)
[111]	0.9	1.8551(0.0988)	0.9949(0.0006)	0.0411(0.0044)	12.4000(0.8492)	1.8587(0.1025)	0.9128(0.0008)	0.1689(0.0098)	41.4600(1.0054)
[111]	1.0	1.8712(0.0838)	0.9824(0.0006)	0.0473(0.0035)	13.0600(0.6879)	1.8609(0.1102)	0.8528(0.0014)	0.4551(0.0323)	49.8600(0.0000)